iLens Interferometer Probing Micro-scale Systems

Ayush Tyagi

A dissertation submitted for the partial fulfilment of BS-MS dual degree in Science

Indian Institute of Science Education and Research Mohali

June 2020

This page is intentionally left blank.

Certificate of Examination

This is to certify that the dissertation titled **"iLens Interferometer Probing Micro-scale Systems"** submitted by **Mr. Ayush Tyagi** (Reg. No. MS15202) for the partial fulfilment of BS-MS dual degree programme of the Institute, has been examined by the thesis committee duly appointed by the Institute. The committee finds the work done by the candidate satisfactory and recommends that the report be accepted.

Dr. Ananth Venkatesan Dr. Sanjeev Kumar Dr. Kamal P. Singh
(Supervisor)

Dated: June 29, 2020

Declaration

The work presented in this dissertation has been carried out by me under the guidance of Dr. Kamal P. Singh at the Indian Institute of Science Education and Research Mohali.

This work has not been submitted in part or in full for a degree, a diploma, or a fellowship to any other university or institute. Whenever contributions of others are involved, every effort is made to indicate this clearly, with due acknowledgement of collaborative research and discussions. This thesis is a bonafide record of original work done by me and all sources listed within have been detailed in the bibliography.

Ayush Tyagi
(Candidate)

Dated: June 29, 2020

In my capacity as the supervisor of the candidate's project work, I certify that the above statements by the candidate are true to the best of my knowledge.

Dr. Kamal P. Singh
(Supervisor)

Acknowledgements

I would like to take this opportunity to convey my acknowledgements to every individual who has helped me for the past few years to inch towards my research goal.

First and foremost, I would like to express my sincere gratitude to my supervisor, Dr. Kamal P. Singh for his guidance and support. His resourcefulness ensured having all experimental means at my disposal which enabled me to design and implement the various experiments at will. His valuable insights and constant vigilance at every stage of the project has helped me to perform better and work harder.

I would also like to thank Ms. Pooja Munjal for her numerous contributions that were helpful in conducting the experiments. Her constructive comments and motivation throughout the project is greatly acknowledged.

My heartfelt thanks to the members of Femtosecond Laser Lab for their moral support, discussions and indispensable help during difficult experiments and all the fun times.

Finally, I would like to acknowledge my family for their love and support, and all my dear friends for having faith in me, constantly motivating and thus bringing out the best in me.

Ayush Tyagi

Abstract

Studying light and matter interaction using optical techniques happens to be of great importance in various science and technological fields. This is because the field of optics offers a wide range of applications as a non-contact metrological tool. It is implemented in devices ranging from optical profilometers, interferometers, spectrographs, temperature sensors etc. One of its major techniques is optical interferometry, which has emerged as a crucial tool for measuring small displacements and surface features with extraordinary precision and speed. This thesis presents an interferometry based optical metrological technique used to carry out sensitive measurements of thermo-mechanical dynamics experienced by microscale objects.

The experimental method presented here for optically probing thermo-mechanical strain in fibre-like microscale systems is demonstrated on a thin silver (Ag) wire specimen and on a human scalp-hair specimen. While focused laser beams are used to irradiate these specimens, central technique to the complete experimental system is the iLens interferometer. Studies of temporal profile of dynamic interference fringes are carried out using the superposition principle of light waves. Theoretical and computational analysis of the interferometric fringes led to the development of convenient computer programs to extract explicit dynamical information out of the system. Further modifications in the interferometric probing system are introduced to enable the study of additional physical properties of the microscale systems, like response time etc.

Optical interferometry provides sensitive metrological capabilities and can be applied to various other science and engineering fields, for instance, in biology and medicine to measure subcellular components, making use of its non-invasive nature of application. Also, it finds a variety of uses in mechanical testings of microelectromechanical systems (MEMS) and materials such as thin films, micro-tubes, cellular biomaterials etc. As part of the future scope of the research presented in this thesis, it includes a few experiments to measure the mechanical response delay of thin microfibres. Results of these experiments are left without much of a rigorous analysis since these were meant to test a few of the wide range of possible applications towards

which this research work can be extended. Application of the experimental method presented in this thesis can also be further extended to test many ultra-thin natural biopolymers exhibiting high mechanical advantages that can have a vast variety of applications, such as in designing components of micromachines.

Contents

List of Figures

List of Tables

List of Abbreviations

Acronym	**W**hat (it) **S**tands **F**or
MEMS	**M**icro-**E**lectro**m**echanical **S**ystems
CCD	**C**harge **C**oupled **D**evice
CMOS	**C**omplimentary **M**etal **O**xide **S**emiconductor
IDM	**I**nterferometric **D**ynamic **M**easurement
BS	**B**eam **S**plitter
PD	**P**hoto-**D**iode
CW	**C**ontinuous **W**ave
PZT	**P**ie**z**oelctric **T**ransducer
T/R	**T**ransmittance/**R**eflectance
ND	**N**eutral **D**ensity
PLD	**P**ath **L**ength **D**ifference
s	Subscript for **s**ample
r	Subscript for **r**eference

Notations

Notation	Name
λ	Wavelength
f	Focal length
z_1, z_2	Optical path lengths
δ	Deflection
ϕ	Cross-sectional diameter
ω	Gaussian beam radius

Chapter 1

Introduction

Interferometry has rendered itself as an indispensable tool for many fundamental techniques in optical metrology. It helps in carrying out the most sensitive measurements with extraordinary precision and speed, and therefore has applications in a vast variety of fields ranging from spectroscopy and astronomy to nuclear and particle physics [1, 2, 3]. This thesis presents a novel optical interferometry technique used to track detailed dynamics of microscale objects. It is followed by the development of signal processing algorithms which facilitates the post-acquisition static data conversion process and other experimental variations towards the end. Following is an overview of the various steps involved.

The first chapter provides a holistic description of the ideas behind interferometry and microscale material systems. Scaling effects from macroscale to microscale are discussed which sheds light on the relative importance of same physical forces when applied to both of these sizes of systems. Challenges in characterising small-scale material properties that are often related to preparation and handling of microspecimens [4]. Also, the advantages and applications of growing miniaturisation techniques in a variety of microsystems are discussed. A brief introduction to the basic principles of optical interferometry techniques along with its applications in microscale systems is discussed, with a focus on iLens interferometry and its suitability in accomplishing the goals of this thesis. This novel home built technique is capable of achieving picometer-scale precision homodyne interferometry on random surfaces while making the system significantly compact. It miniaturises the interferometer design by integrating the functions of three optical elements into one single lens (called the iLens or the interferometer lens) [5].

The development of an iLens interferometry based experimental method to mea-

sure microscale sample dynamics is presented in Chapter 2. A detailed description of system components and design is followed by calibration of the interferometer against a known sample motion. This includes theoretical studies of the underlying interference principle and methods to characterise the light waves as they undergo various optical phenomena. A silver wire (15 μm diameter) and a hair fibre (100 μm diameter) sample were used to demonstrate the working of experimental setup as they were exposed to a focused pump laser radiation of varying power and exposure time. The interference intensity signal corresponding to the motion of the samples were recorded which contains the dynamical information about them needed to be decoded in order to get analysed.

The next crucial step required in the process is developing a robust method for interferometric dynamic measurements, i.e. processing and analysing the output interference signal to measure the change in optical path length as a result of motion, deformation or uneven surface features of an object. This begins with formulating a general expression that relates each step displacement to the intensity change at the point of detection in Chapter 3. Multiple phase extraction algorithms are then developed and applied over a common test signal simulated for some fixed experimental parameters which compares them over their respective errors. The most efficient method is then used to convert results from previous chapter into their corresponding displacement plots that helps in representing and analysing the dynamics of the microscale samples with changing experimental parameters.

The research work presented here is centred around the application of optical interferometry in microscale materials. Hence its holistic description requires a brief discussion about the idea behind interferometry and microscale material systems. Aim of this chapter is to present such an introductory overview of these topics with view of their later experimental requirements in mind.

1.1 Microscale systems

Changes in the characteristic size of a system changes the way in which its physical problems are handled. Scaling down from macroscale to microscale makes significant changes in relative importance of the same physical forces applied to both the systems. Macroscale testings of materials has been a dominating research area in the early era of industrial revolution. But in the 1980s, the advent of micro-electromechanical systems (MEMS) and its rapid development resulted in an increasing demand for research

in micro/nanoscale material phenomena and dealing with its basic challenges (like fabrication of specimen, high-resolution force and displacement sensing) [6]. Evidences supporting the development of characterisation tools for such systems is well established as comprehensive reviews in literature [7, 8, 9]. This section is an attempt to describe the broad features of microscale systems and to provide a basis to deal with some of its underlying issues.

1.1.1 Classification as microscale

These are the materials having at least one dimension at the length scale in the range of 1-1000 microns. The size at which elementary mechanisms occur. It could be a three dimensional (3-D) bulk matter with ultra-fine grains, two dimensional (2-D) material like thin films of microscale thickness, one dimensional (1-D) microtubes and microwires with cross-sectional diameter of the order of few tens of microns, or even cellular biological materials. But can someone try to classify microsystems by simply looking at their size? For example, a range of 1 μm to 100 μm could also be postulated. Though it is clear that the system size remains as a significant factor in this classification, an exclusively size-based approach is still quite doubtful. To classify microscale materials, and systems whose micro-structural feature sizes are of the same order as material's structural dimensions, one should also study the basic physical laws to be applied, major phenomena and the fabrication process used while it is tested.

We will continue here with adding some of the distinctive theoretical enhancements that are to be made or are encountered while handling physical problems at small scale.

Small Surface Area-to-Volume (SA/V) ratio

It can be easily seen that, at microscale, the system's volume is significantly smaller for smaller lengths. Also, it decreases more rapidly than the decrement in its surface area which in turn makes the surface area to volume ratio much sensitive at this scale. It is a state when even a slight decrease in length lead to drastic increment in this ratio. And since physical properties like heat transfer through a material into its surroundings happens across the surface area, it creates a large deviation in them [10]. Also for mass transfer, in a similar fashion, very steep heat and mass transfer gradients form within the system at microscale due to this large change.

Similarly, for other phenomena important at microscale, there are scaling laws which

shows how the system behaviour changes at microscale.

Scaling Laws

Scaling laws are rules that bridges the gap in predicting how a physical system will behave between macroscale and microscale. Broadly, volume dependent forces such as inertia and gravity decrease faster than dependent forces such as friction and adhesion [11]. A common parameter of interest can be identified to scale such forces.

However, the forces are not often of direct importance. For mechanical systems, response time is also an important parameter. This is determined from the transit time, $t = \sqrt{(2xm/F)}$ where, x is the distance that needs to be travelled, m is the mass and F is the force. The scaling law for the response time can be calculated as, $t' = s^{\frac{4-f}{2}}t$. The scaling law for the force, s^f here has been left generic. The scaling law exponent of response time is ideally greater than zero, indicating that as the system is miniaturised its response time is decreased with also a clear dependency on the force's scaling law.

1.1.2 Challenges in microscale testing

Efforts to characterise small-scale material properties and to develop their microscale experiments face significant challenges that are related to the preparation and handling of microspecimens, controlling the amount of force applied to deform them and their accurate stress and strain measurements [4]. They all must be overcome to measure mechanical behaviour and properties of these microspecimens reliably.

Various testing techniques have been developed to measure mechanical response of such small specimens. An in-depth review on such techniques is covered in [12]. Handling difficulties associated with small specimens and a need for on-chip testing of MEMS devices has led investigators to consider methods other than the typical instrumented indentation technique [13]. It also supports the fact that despite having multiple models proposed, strength and strain cannot be directly measured with indentation techniques.

It is often observed with tensile specimens which require large forces to produce small axial elongations, that a much larger deflection at lower loads can be produced using cantilever beams. Bending measurements of such systems can also be used to measure the material's strength since deviation beyond its elastic response will produce localised deformation or fracture [14]. However, the accuracy of the measurements of

all indirect techniques depends a lot on the boundary conditions and geometry of the microscale beam, and this uncertainty comes in as a huge challenge to the use of these techniques. Processes similar to these found in microelectronics industry are followed by the ones used to prepare MEMS test specimens. They can be broadly stated as the material deposition on a substrate followed by photolithographic specimen patterning and etching. Explained by Sharpe et al. [15] in detail. The specimen prepared in such a case is easy to handle and enables both Young's modulus and Poisson's ratio measurements. Also, thicker specimens of MEMS materials can be prepared by electroplating metal alloys like Ni into moulds to make robust micro-tensile specimens that can be handled with tweezers.

Regarding force application and measurement, there are commercially available load cells with 5 g force range and 0.001 g resolution which can be used to measure force on small specimens. Also, the displacement of its end can be achieved by attaching it to a load cell and using precision piezoelectric or screw-driven displacement stages. Measurements can be made about overall motion of the movable grip or holder using capacitance probes that can achieve a resolution of 10 nm [16], but still the estimation of strain from these measurements remains a challenge because of the complying load cell and localised plasticity in specimen's shoulders. Moreover, loading micro-compression specimen can also produce other unique challenges regarding buckling and alignment. Determining strain from grip displacement becomes complicated because of the compliance of the testing setup. In such cases, either the sufficiently different compliances are subtracted out from specimens of different length and width or other indirect methods measuring tensile strain are used. For instance, tensile tests shown by Espinosa et al. [17] are created by taking a long and narrow strip of Au film which is fixed at each end and its centre is pushed. Optical interferometry technique is then used to measure the vertical deflection along the strip and is then converted into its elongation.

1.1.3 Advantages and applications

Growing miniaturisation techniques are potential key steps for the future that will give rise to completely different ways in which people and machines interact with each other and with the physical world. It has emerged leading the fields of microscale science which are in turn used to examine the new physical and chemical phenomena exclusive to this scale and to be utilised for the development of a variety of microsystems. The unique physical environment under which most of the microscale systems operate, helps in using them for low-cost , portable and suitable for point-of-care

applications. Some intrinsic features of such systems, for instance very sharp heat and mass transfer gradients can be attributed to its surface area to volume ratio and its high scaling nature. This has numerous applications in research and industry based processes like determining variations of the thermo-physical properties of such devices and their related operational behaviour at different temperature levels [18].

The core areas that can be emphasised under the paradigm of Microscience, engineering and technology are [19] :-

- Fundamentals of microscale science and engineering: Providing a coherent critical understanding of phenomena and effects in materials at microscale.
- Microsystems and Micro-devices (organic, inorganic and hybrid): Designing and implementing new structures, systems and devices exhibiting novel properties and utilising these novel phenomena and effects.
- Micro-materials and Micro-fabrication (micro-technologies, processes, materials and techniques): Having to control and manipulate the matter at microscale for precise fabrication of advanced and novel systems and devices.

Applications of miniaturised devices with mechanical components having features in the range of a few to few hundreds of microns span the fields that include optics, communications, electronics, biotechnology and medicine to name a few, not to mention the growth in research activities in regard to MEMS in the past three decades. That is a reason why mechanical testing of materials such as thin films, microtubes, microwires and cellular biomaterials becomes essential for commercialisation and development of microscale integrated systems. The research work presented in this thesis thus tries to cover one such part of these testings.

1.2 Interferometry techniques

After a brief description of microscale systems and its features, the dire necessity of a suitable metrological tool for a three-dimensional analysis of its microscale components is quite unambiguous. The tools and techniques that are currently available to serve the purpose of small force and displacement measurements can be broadly classified into contact methods and non-contact methods. This section provides a brief description of optical interferometry as one of those non-contact methods in general, and its application and feasibility in regard to microscale systems in particular.

Having its roots in the famous double-slit experiment conducted by Thomas Young in the early 1800s, the first interferometer was developed by Albert Michelson and Edward Morley in 1887 [20] which they used to make a very reliable estimate of the speed of light. This experiment opened up an entirely new paradigm in metrology, where light could be used as an absolute standard of measurement [21]. Since then, interferometers have become a widely used tool for measuring small displacements and surface features in Science and Engineering.

1.2.1 Basic principle

The underlying concept of interferometry is to somehow convert the phase information from an electromagnetic radiation source, which we cannot sense directly, to intensity information, that can be detected. A linear interferometer thus combines two beams from a same source and their relative phase is then used to extract information about the difference in their optical path lengths. Despite having many interferometer designs around, like the Fizeau interferometer, the Mach-Zehnder interferometer and the diffraction grating interferometer, the original Michelson interferometer configuration is enough to explain their fundamental principle.

In a typical Michelson interferometer, a monochromatic light source is divided into two perpendicular beams using a beamsplitter. After getting reflected off of two mirrors, at normal incidence, the reflected beams recombine again at the beamsplitter and then gets reflected towards the detector where their resultant intensity is measured. The resulting intensity pattern of the two superimposed beams thus formed over the detector is known as an interferogram.

Combination of waves from two coherent sources results in interference. It utilises the theory of superposition to create a distance measurement, as explained analytically in Section 2.2. If the two superimposed signals are perfectly in phase, the resulting interference signal will be purely constructive (Fig. 1.1a) and if the two signals are 180° out of phase, the interference is purely destructive, with no intensity falling on the detector (Fig. 1.1b). The path difference between the two beams when one beam travels unequal distance than the other, results in a phase difference in the interferometer. For every half a wavelength of path difference, the interference signal reaches a trough (destructive interference) and similarly, it reaches an intensity peak point for every other half a wavelength of path difference. This entire sinusoidal intensity curve is called the interference curve and is basis for all interferometric metrological techniques. The two interfering light beams when directed to a flat screen,

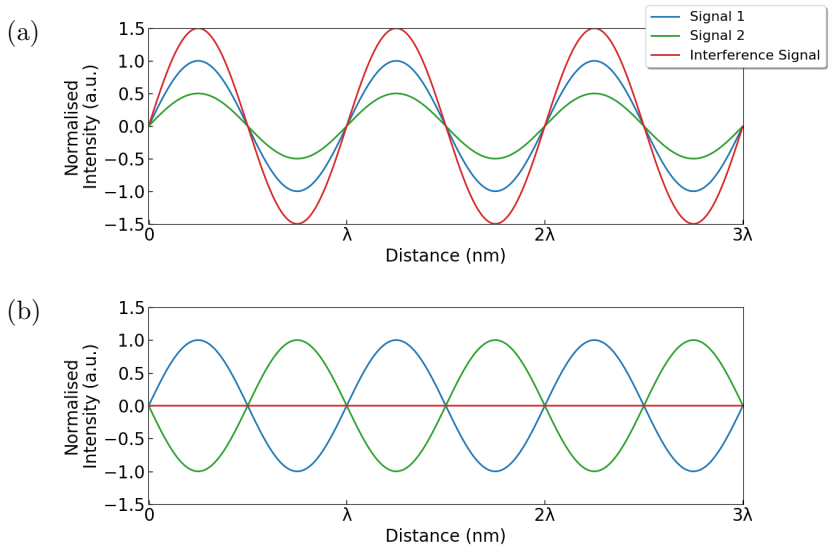

Figure 1.1: **Interference of two sinusoidal light wave signals.** (a) Constructive interference. (b) Destructive interference

forms interference fringes, an evenly spaced pattern of alternating bright and dark light bands.

1.2.2 Application in microscale systems

There are a number of non-contact methods that have been developed for microscale metrology. First and foremost, a standard optical microscope that can measure lateral dimensions but provides no measurements in the out-of-plane dimension. Confocal laser microscopy, however, can provide some information in this dimension utilising a significant number of image processing and interpolation techniques to generate the image. Another useful tool is the scanning electron microscope (SEM) that can provide high contrast 2-D images image with a very high resolution of the order of few angstroms, but still lacks the capability of a true 3-D image generation.

Interferometry on the other hand, uses a variety of phase quantification techniques between two or more coherent light beams to achieve a sub-nanometer level resolution in the vertical direction. Phase-shifting interferometry (PSI) is typically used to test smooth surfaces with very high accuracy. The only downside it has is that it is limited to a definite vertical step limit of one quarter of the used wavelength [22]. A change in height of more than this limit due to high surface roughness results in a very dense fringe shift patterns that can sometimes lead to a skipped fringe cycle, known as the 2π error. Therefore, for rough surfaces, a better suited and more efficient white-light Vertical-scanning interferometry (VSI) is used. It aims at quantifying the phase information

from the interferogram using the contrast of fringes which gives a nanometer range precision rather than the sub-nanometer range provided by PSI. However, due to a wide spectral bandwidth of the source, VSI has short coherence length. Conclusively, VSI has a wider dynamic range but lower resolution, whereas PSI has excellent resolution but limited dynamic range. However, there are also methods that combine the aspects of both the techniques to take advantage of the strength of each approach [23]. These often fall under the name of White-light phase-shifting interferometry or enhanced VSI.

One of the main applications of interferometry is for high precision surface metrology. Instantaneous information about surface roughness and waviness with angstrom level vertical resolution and high lateral resolution can be obtained by PSI, which is therefore typically used to characterise high-quality surfaces. Whereas, VSI can characterise surfaces with larger discontinuities such as steps and cavities. Its long range vertical measuring ability, that is accurate down to single nanometers makes it well suited for applications in MEMS and semiconductor measurements. In the fields of biology and medicine, it serves as a versatile measurement tool for cells, tissues, biomaterials and other subcellular components [24]. Other areas of application for this method covers integrated optical circuits, precision machined surfaces etc. The enhanced VSI technique can measure surface of microlenses and microlens arrays that are essential components of modern fibre optic network devices, with its high resolution and repeatability similar to PSI.

1.2.3 iLens interferometer

Often, the high precision interferometry techniques mentioned above in this section make use of multiple optical components of high-quality build which makes them bulky and expensive. They can suffer significant compromises regarding fringe-contrast when used for probing arbitrary surfaces [25]. Whereas, the novel technique mentioned here, home-built in the Femtosecond Laser Lab at IISER Mohali, is capable of achieving picometer scale precision in homodyne interferometry on random surfaces while making the system significantly compact [5]. The advantages and versatility of this newly developed technique is exploited throughout later chapters since it has a primary use as the probing mechanism in the system described in Chapter 2.

A partially silver-coated convex lens, or the interferometer lens (iLens), as it will be referred to throughout this text, is at the heart of the interferometer setup. It miniaturises the interferometer by integrating functions of three essential optical

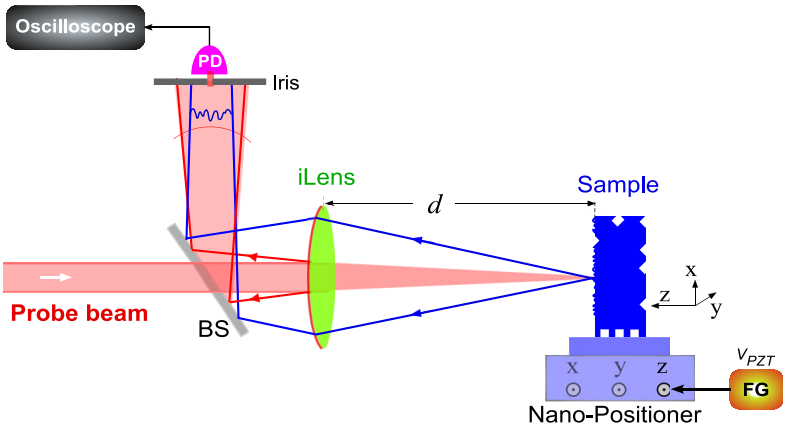

Figure 1.2: **Schematics of iLens interferometer.** A piezo-positioner driven by V_{PZT} from a function generator (FG) controls the distance $d(t)$ of sample from the iLens. A photodiode (PD) detects the central intensity of fringes.
Source: [5]

elements, the beam splitter, reference mirror and a light collection element into a single lens. Schematics of the experimental setup is shown in Fig. 1.2. The sample is kept at a distance d from the iLens. Reflected beam from the sample and the reference beam are superimposed collinearly to produce the interference pattern which can be recorded using a photodiode (PD). The iLens interferometer works with a wide variety of common surfaces, most of which are readily available materials like cloth, paper, wood, plastic, metal, human skin etc. to produce high-contrast stable fringes. Different sample properties like their surface roughness and curvature determines the fringe shape. Nevertheless, for all the samples the interference contrast (C) was between 70 - 95%, which can be calculated using,

$$C = \frac{I_{max} - I_{min}}{I_{max} + I_{min}}$$

where, I_{max} and I_{min} are the maximum and minimum light intensities of the interference fringes respectively. An appropriate lens coating can be used for different samples according to their reflectivity to obtain optimal fringe contrast. Interference intensity recorded at the centre of fringe pattern ($I(x_0, y_0)$) is equated to the theoretically calculated displacement-dependent intensity $I(d(t))$ to obtain the sample displacement $d(t)$.

1.2.4 Advantages of using iLens technique

The versatility of iLens interferometer as highly sensitive and precise displacement measurement system can be recognised by appreciating its uncompromised application

on various common surfaces. The simplicity and compactness of the setup helps in improving the scanning speed and the signal processing algorithms. Less components means more stability, which allows for an increment in the signal-to-noise ratio in view of the noise arising from non-fundamental mechanical or thermal sources. Also, since the system intrinsically provides displacement measurement functionality, it can be self-calibrated by giving an input displacement $\Delta d = d(t) - d(0)$, to the sample using a nano-positioner and then comparing this applied displacement with the one acquired from the system.

This technique can measure dynamic displacement of arbitrary surfaces with sub-20 pm precision even with a cardboard surface. This level of sensitivity can find its application in surface topology of small objects and systems or mechanical motion tracking of small parts of MEMS and other organic or inorganic microscale systems. Demonstrated examples of such high precision devices that are using this technique is shown in [5]. It includes a paper-based optical balance that can carry out fast weight measurements with sub-100 pg accuracy, and an ultrasonic acoustic sensor achieving broadband detection (1 Hz to 200 kHz) with higher sensitivity for weak driving amplitudes when compared to its commercially available counterparts.

Chapter 2

iLens based nano-dynamics tracker

The ability to rapidly obtain nano-meter resolved spatial information is essential for high precision surface metrology and dynamical tracking of small scale mechanical systems. Two popular optical methods to achieve this are Phase shifting interferometry (PSI) and Vertical scanning interferometry (VSI). However, challenges in high-speed scanning cause significant compromises in these techniques when it comes to wide-range applicative ability. In addition to the investment cost of multiple high-quality optical components, they lack enough versatility to be used for samples of extreme geometries with consistent accuracy.

Direct homodyne interferometry still remains in popularity since it greatly addresses the stability issues and complex algorithms that accompany other high precision techniques. As discussed in chapter 1.2, iLens interferometry technique miniaturises the interferometer design by incorporating the functions of a beam splitter, reference mirror and light collector within a single optical element which results in high-contrast, stable fringes from a variety of common material surfaces. It has recently been used to probe acrylic and rough graphene oxide surfaces for their deformation dynamics with upto 150 *pm* precision [26]. Using temporal variations in intensity at the centre of interference fringe pattern, this technique measures the quick movements of the sample surface.

In this chapter, an experimental method is presented for optically inducing thermo-mechanical strain in fibre-like microscale systems, central to which is an iLens interferometer to capture their dynamical response. Additionally, a small variation to allow for similar measurements for relatively thicker samples is shown. This opens up a possibility of its application for a very precise topological study of micro-objects.

2.1 Pump-probe experimental setup

The schematic diagram of the interference system is shown in Fig. 2.1. The experimental setup consists of a low-power collimated He-Ne laser source as the probe. Using an arrangement of mirrors, the incoming laser beam is passed to the iLens after going through a beam splitter. iLens is essentially a partially silver-coated convex lens which works as a single element interferometer. It divides the incoming probe beam into a reference beam and an object beam. The object beam propagating along the positive z-axis is allowed to fall laterally on the sample, from where its scattered reflection is again collected by the iLens. It then combines with the reference beam and gets reflected from the beam splitter to project the high-contrast interference fringes over the detection elements. The above arrangement makes up the probing arm of the setup.

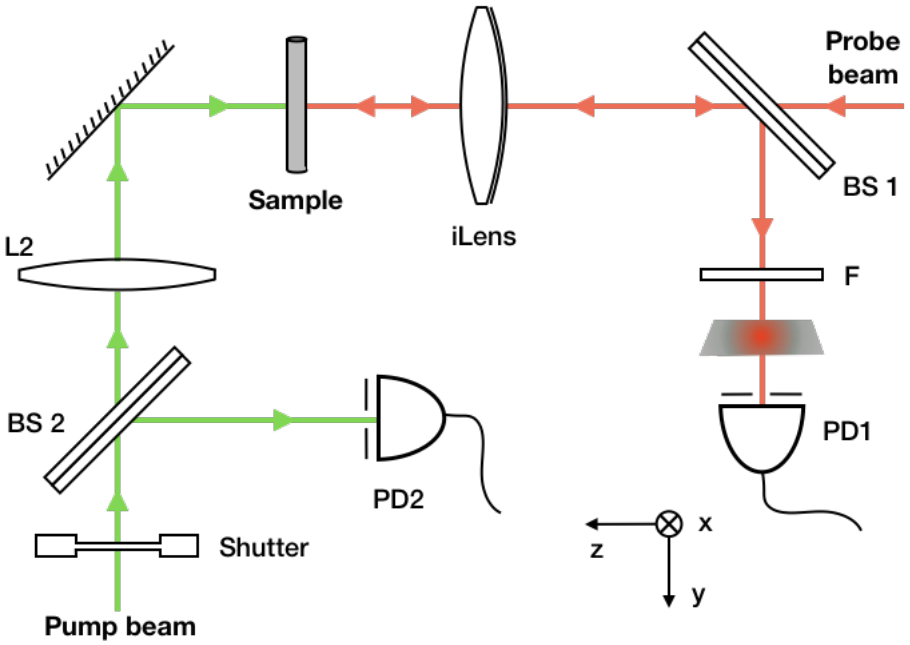

Figure 2.1: **Schematics of the experimental setup.** A focused pump beam ($\lambda = 532\ nm$) hits the sample along the z-axis to displace it or deform it locally. These movements are read by the probing arm using a He-Ne laser ($\lambda = 635\ nm$) to produce the interference fringes. PD1 and PD2 simultaneously detects the fringe intensity and pump pulse respectively.

Local perturbations were induced in the sample using a focused pump laser operating in low to medium power ranges. This CW laser beam is allowed to pass through a precisely controlled mechanical shutter to generate short pulses of varying exposure times. A converging lens was used to focus the beam over the sample, hitting it laterally on the back, in the direction opposing the probe beam (negative z-axis).

Before focusing, a beam splitter reflects a part of this beam towards a photodiode PD2 through a narrow iris opening to record the pulses. Description of individual components of probe arm and pump arm is as follows:

-Probe Arm-

- **Laser:** A 635 nm (red) He-Ne gas laser module was used as the probing source. The low-power continuous wave output of this module remained at 2 mW. The output beam is randomly polarised with its $1/e^2$ diameter $\approx$ 1 mm.

- **BS1:** The beam splitter used in the probing arm is a 2-inch circular plate-type beam splitter. Working at 45° incidence angle, it gives a 90/10 T/R ratio.

- **iLens:** It is a partially silver-coated bi-convex lens ($f = 1$ cm) having its coating face towards the incoming source light (60/40 T/R ratio). To deal with microscale samples, a low-aperture lens is taken, with 1/2-inch diameter.

- **F:** Filter. A 650 $nm \pm 40$ nm band pass filter is attached after BS1 which blocks the unwanted pump light from interrupting the detection.

- **PD1:** Photodiode. The filtered interference light passes through iris to reach the photodiode. It has a sensor size of 0.8 mm^2. It returns an electrical output signal measured in Volts(V) which is read using an oscilloscope and is directly proportional to the intensity of light falling over the small area integral of its sensor.

-Pump Arm-

- **Laser:** A CW solid-state laser module ($\lambda = 532$ nm) was used as the pumping source. Its output power was varied from as low as 0.5 mW upto 42 mW. More about the size and shape of pump beam is discussed in the next section.

- **Shutter:** This is a 1-inch diaphragm shutter controlled using a shutter controller from Thorlabs. Attached right after the laser output, it creates the pump beam pulses with desired pulse-widths.

- **BS2:** Beam splitter used in the pump arm. A 1-inch circular plate-type beam splitter with 50/50 T/R ratio. It reflects a part of the incoming pump beam towards the photodiode for detection.

- **L2:** This is a 1-inch bi-convex lens with focal length of 12.5 cm to focus the pump beam onto a desired spot over the sample. Paired with an adjustable mirror, the position of pump spot is set.

- **PD2:** A second photodiode along with a small iris opening is used to record the pump pulses. It has a sensor size of 0.8 mm^2 and works in a similar way as PD1. A suitable ND filter is also attached before it whenever the pump beam power is raised.

The changes in the sample as reflected by its surface are observed using the interference fringes formed on the screen. A typical example of such fringes is shown in Fig. 2.2b. An oscilloscope records the intensity at the centre of these fringes using the photodiode PD1. Simultaneously, the other photodiode PD2 captures the pump light to track its 'on' and 'off' transitions. Intensity oscillations as a result of fringe evolution at PD1 are processed using appropriate algorithms (details about the signal processing algorithms in chapter 3.2) to extract the dynamics at the outer sample surface.

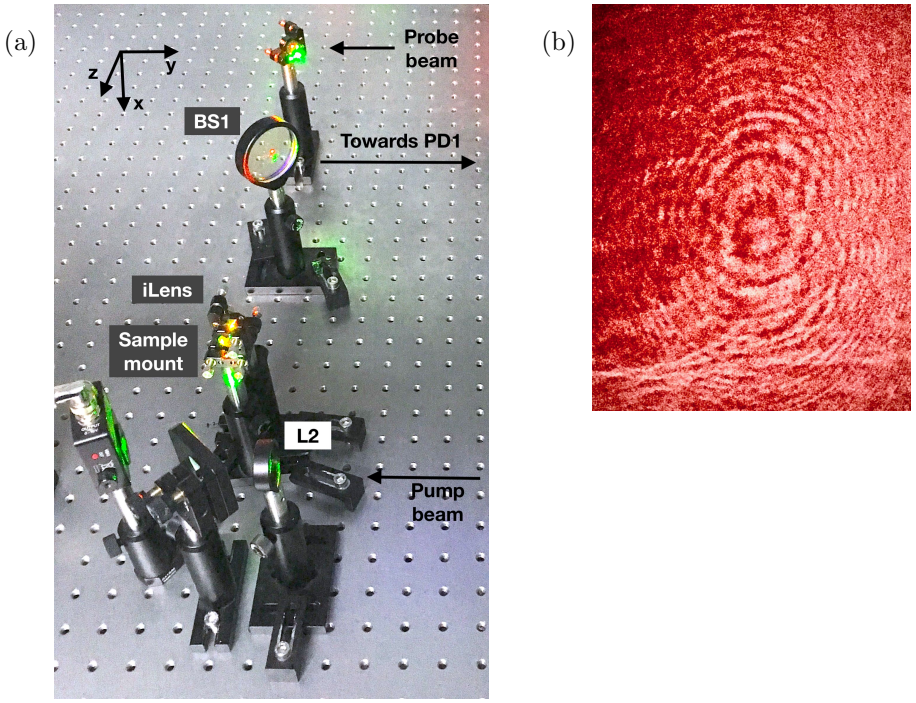

Figure 2.2: **Annotated picture of the experimental setup and image of the interference fringes.** (a) The various optical components and their abbreviations are described in the text. (b) Fringes are obtained from a silver microwire sample as mentioned in the demonstration.

Test samples and mounting

This study aims at probing the nano-mechanical dynamics of microscale material systems. Thus the test specimens used were all of thin fibre-like shape with circular cross-section maintaining the azimuthal uniformity. Axial dimension of the samples was constant throughout, determined by the holding position of their common mount which is 1.5 cm, whereas the radial dimensions are of microscale orders. There were two samples, an organic and an inorganic, used for the experiment:

- Silver (Ag) wire, cross-sectional diameter (ϕ)= 15 μm
- Human scalp hair fibre (Black), $\phi = 100$ μm

Since both the samples are flexible fibres, they are affixed to a plastic holder that mounts them onto a post. As discussed in section 1.1, various handling difficulties are associated with small specimens. The use of a dedicated holder helps in rectifying many such issues in this case.

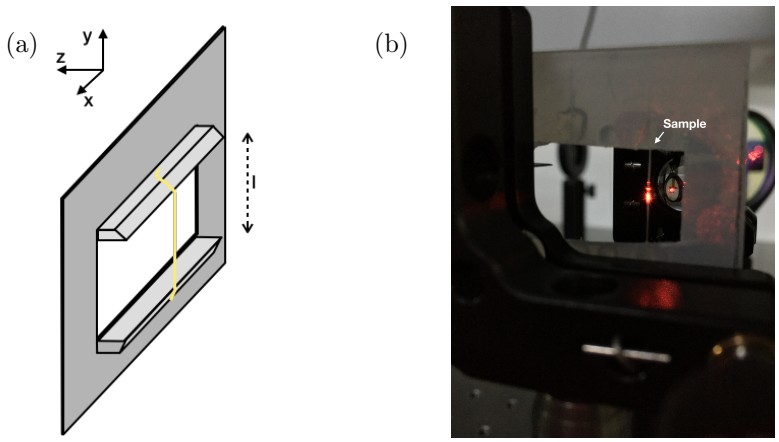

Figure 2.3: **Schematic diagram depicting sample mounting and its orientation.** (a) The holder mounts the sample on a post to maintain a fixed position and orientation of its end points. (b) Picture from back of the sample holder while the probe beam hits the centre of the sample.

Ends of the sample are glued to the outer faces of the two wedge-shaped protrusions on the holder as shown in Fig. 2.3a. This vertical distance between their extreme edges thus becomes the essential length of the sample which is l (= 15 mm). Both these wedges makes the sample behave as a fixed-ended beam kept vertically along the y-axis and positioned in the two coinciding focal planes of iLens and L2.

Alternate configuration for thicker samples

While the above described setup (Fig. 2.1) serves the purpose of testing subjects with microscale dimensions, a small change in it allows for putting in thicker material fibres to test too. The underlying condition for the pump beam to provide a uniform irradiance over a section of sample's length is that its focal spot should entirely cover the width (cross-sectional diameter) of the sample in that section. In case of thick fibres (ϕ of around a few hundreds of microns or a few milimeters), this could be achieved by removing the lens L2 to let the unfocused pump beam to fall on the sample. No change in the probing arm is required since this interferometry technique uses a small surface patch for its measurements which is adequately available in larger samples.

This configuration thus helps in increasing the area of pump irradiance without disturbing other elements of the setup. For instance, a piece of copper wire ($\phi = 720\ \mu m$) was also experimented under this modified setup to test its feasibility to adapt for a wider range of objects. However, all further study presented in this dissertation is carried on the two main samples (Ag microwire and hair fibre) using the original setup with focused pump beam.

2.2 Calibration and beam characterisation

Before moving on to perform experiments with the complete pump-probe setup, the focal spot of pump beam was experimentally characterised and interference intensity distribution of probe beam was studied to ensure that the light-matter interactions eventuating in the process are known well enough and to frame a basis for analysing the generated interference signal.

This section covers the spatial aspects of beam characterisation for pump laser in relation to its exposure on the sample and discusses the formalism required for interference intensity calculations of probe beam that is to be used for setup calibration and signal conversion.

2.2.1 Pump beam

Pump beam originates from a solid-state laser source of wavelength 532 nm. It passes through a converging lens L2 and focuses onto the sample kept at $f = 12.5\ cm$ away

from L2. A CCD camera beam-profiler (BC106-VIS from Thorlabs) was placed directly in the beam path at the following two positions: (1) Focal plane of L2 (Sample position) and (2) Between BS2 and L2. Images of its transverse profile were captured by the profiler while translating it through a small distance along the z-axis at position 1 and at a random location at position 2. The orthogonal views shown in Fig. 2.4 are thus obtained.

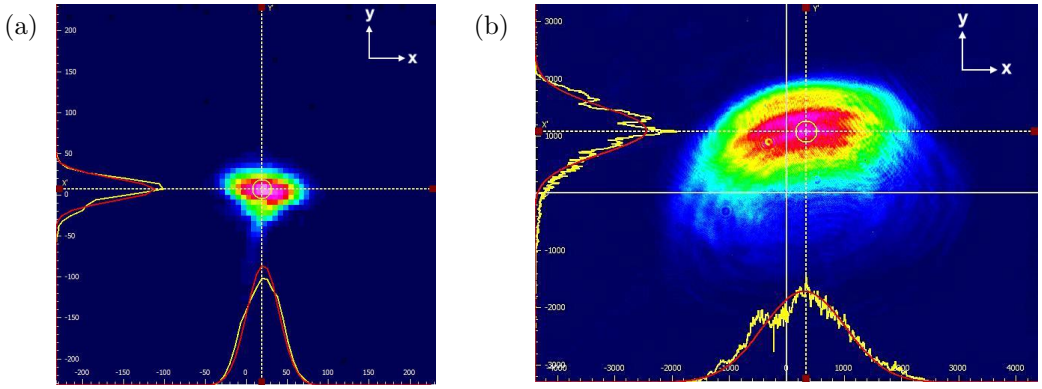

Figure 2.4: **Pump beam characterisation profiles.** (a) Beam profile in the xy-plane at position 1. (b) Beam profile in the xy-plane at position 2. Intensity profile for both the images along the dotted lines in x- and y-direction are shown in yellow. Their corresponding gaussian fits are in red. Both the x- and y-axis runs in units of μm.

Tabulated data of gaussian diameter of beam at both the positions is given in Table 2.1 along with other individual fit measurements for X-diameter and Y-diameter. Each of its entry is measure of $1/e^2$ width of the beam. The lateral extension of the beam in x- and y-direction is uneven, resulting in an elliptical shape, but this effect is much less prominent at position 1. A tight focus at position 1 results in a very narrow spatial extension as compared to that at position 2. This is beneficial for irradiating small specimens and to precisely specify the region of irradiance on its surface.

	Gaussian diameter X (μm)	Gaussian diameter Y (μm)	Effective beam diameter (μm)
Position 1	80.2	50.9	67.1
Position 2	2899.6	1632.5	2410.0

Table 2.1: Pump beam widths measured at two different positions on the setup.

Also, the amount of power contained by the pump beam greatly affects the response of the specimen under test. During the experiment, it was varied through a fixed range

to observe variations in its effects. Therefore, it is essential to know the amount of light energy that is being transferred into the sample. One of the initial inspections to compute this, is of the area-ratio of the light energy falling of sample's body to its net output energy per unit time. Given the varying sample widths, there can be two situations that can occur, either the focal spot of pump beam will not cover the entire sample width or it will overshadow the sample's exposed region. Schematics to represent both these cases are shown in Fig. 2.5.

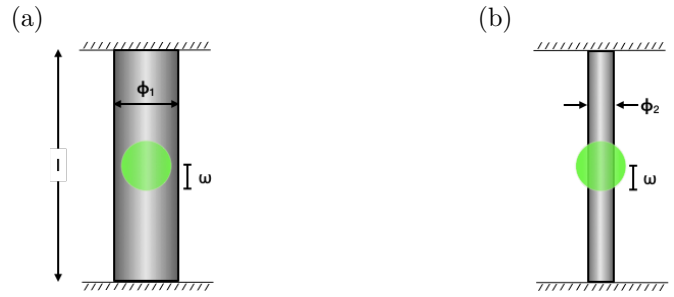

Figure 2.5: **Schematics depicting the area-ratio of pump energy falling on sample.** Green patch represents the focal spot area of pump laser exposing the sample.
(a) Case 1: Sample width (ϕ_1) $\geq$ beam diameter (2ω).
(b) Case 2: Sample width (ϕ_2) $<$ beam diameter (2ω).

As it can be easily seen here, the fraction of pump laser power being used to irradiate the sample is equal to the ratio of the area of pump focal spot that covers the sample to the total area of the focal spot. For Case 1, this factor is 1 since every part of pump laser lies on the sample, whereas, for Case 2, this is given by,

$$\text{area-ratio} = \frac{2}{\pi}(p\sqrt{1-p^2} + sin^{-1}p) \tag{2.1}$$

where $p = \frac{\phi}{2\omega}$, ϕ is the sample width and ω is the gaussian beam radius of pump laser at its focus. This area-ratio factor can be multiplied to the total pump laser power to obtain its net effective power on the sample.

Since, the study presented in this text uses the same pump beam structure in every experiment, its $\omega = 33.5\ \mu m$ is constant throughout. Also, knowing the widths of the two samples, the area-ratio factor for silver wire sample ($\phi = 15\ \mu m$), calculated using eq. (2.1) is 0.28 and for hair sample ($\phi = 100\ \mu m$), it is 1. Therefore, there is no need to change the effective pump power for studying the experimental results with hair sample, but the results obtained with silver wire are presented and studied with the

power reduced to 28% of its actual output.

2.2.2 Probe beam

The source of probe beam is a red He-Ne laser of wavelength 635 nm. Its collimated output has a gaussian beam diameter of 1 mm at iLens aperture. The diameter of its focal spot as it gets converged by iLens is theoretically calculated to be around 8 μm. This is done using the equation, $2\omega_f = (4\lambda/\pi)(f/D)$ which calculates the waist diameter of a focused beam, where f is the focal length of the lens, D is the beam diameter illuminating the lens and ω_f is the focal spot radius. Here, low size of the focal spot ensures that no part of the probe laser misses the thin microscale samples while testing, since they are all 15 μm or above at their smallest dimension.

Propagating along the z-axis, the reference beam produced by iLens and the diffuse reflection from the sample combines to form the interference pattern on the detector plane (x, y). Ideally, for the kind of interference system being used, it would lead to an interference pattern like the one shown in Fig. 2.6a with perfectly reflecting object surfaces and unerring optics having no system noise. It displays a series of concentric bright and dark circular bands formed due to the constructive and destructive interference of these two beams respectively. These are called the interference fringes that are liable to change its intensity profile with time as a result of phase change in any of these superimposing light beams. As of our experiment, for instance, the major source of this phase change is the varying path length difference in the two beams caused by displacement or deformation of sample or essentially the displacement of its outer probe-reflecting surface.

The resultant interference intensity is obtained by superimposing the two interfering waves propagating along the z-axis. These two are the reference beam and the sample beam, their electric fields are denoted by $\vec{E}_R$ and $\vec{E}_S$ respectively and have the form,

$$\vec{E}_R = E_{R_0} e^{i(kz_1 - \omega t)} \tag{2.2}$$

$$\vec{E}_S = E_{S_0} e^{i(kz_2 - \omega t + \xi(x,y))} \tag{2.3}$$

where E_{R_0} and E_{S_0} are the maximum amplitudes of both the waves, $k = 2\pi/\lambda$, ω is the angular frequency, z_1 and z_2 are the optical path lengths covered by both the beams and $\xi(x, y)$ denotes the random phase difference at different positions in orthogonal plane of sample beam caused by the minute irregularities on sample surface from

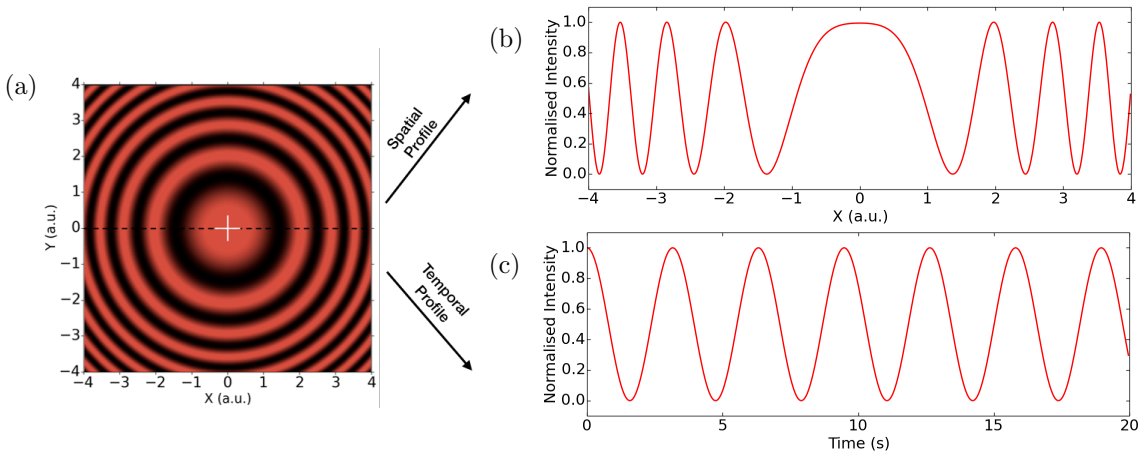

Figure 2.6: **Computer generated time-varying interference fringes of the system.** (a) 2-D interference pattern formed in the detector plane (x, y). (b) Spatial intensity profile at $t = 0$ of the fringes along the dotted line $(y = 0)$. (c) Temporal intensity profile at the centre crosshair corresponding to an arbitrary rate of change of path length difference $(\Delta\dot{d} = 100\ \mu m/s)$.

where the beam appears to originate.

The total intensity $I(x, y)$ can be written as the square of the averaged net electric field $(\vec{E}_{net})$, and using the electric fields given in Eq. 2.2 and 2.3 and assuming $I_0 \equiv I_{R_0} = I_{S_0}$, where I_{R_0} and I_{S_0} are the maximum intensities of the individual fields, $I(x, y)$ becomes (Refer appendix A for its detailed calculations),

$$I(x, y) = 4I_0 cos^2\left[\frac{k(z_2 - z_1) + \xi(x, y)}{2}\right]$$

Now, for measuring the central intensity $I(x_0, y_0)$ at (x_0, y_0), the phase term $\xi(x_0, y_0)$ will remain constant with time, hence it is excluded from the phase difference. Therefore,

$$I(x_0, y_0) = 4I_0 cos^2\left(k\Delta d(t)\right) \tag{2.4}$$

As a result, Eq. 2.4 gives the temporal variations of the interference intensity at centre of the fringe pattern (x_0, y_0). Here $\Delta d(t)$ denotes the sample displacement, which implies that $2\Delta d$ becomes equal to the change in the time varying optical path length difference (PLD), since the sample beam traverses the same extra path that accounts for the PLD, twice. Fig. 2.6c shows an example of such temporal profile where the rate of change of displacement $\Delta\dot{d} = 100\ \mu m/s$ for a light having $\lambda = 635\ nm$. This makes the explicitly time-dependent equation for central intensity as:-

$$\tilde{I}(x_0, y_0) = cos^2 \left[\left(\frac{2\pi \Delta \dot{d}}{\lambda} \right) t \right]$$

where $\tilde{I}(x_0, y_0)$ is the normalised intensity.

2.2.3 System calibration

The displacement (Δd) of the sample and the change in interference intensity signal as a result, are related by the eq. (2.4). Measurements for both of these quantities were calibrated for the setup by providing a reference modulation in the interference intensity by displacing the sample along the z-axis by a known amount. This was done by replacing the fixed sample mount with a PZT mount, enabled with piezoelectric adjusters to provide precise sample movement. While in linear translation, the sample was exposed to two pump laser pulses at both the increasing and decreasing part of the interferogram (linear regime of the sinusoidal function) to also calibrate the direction of sample's movement.

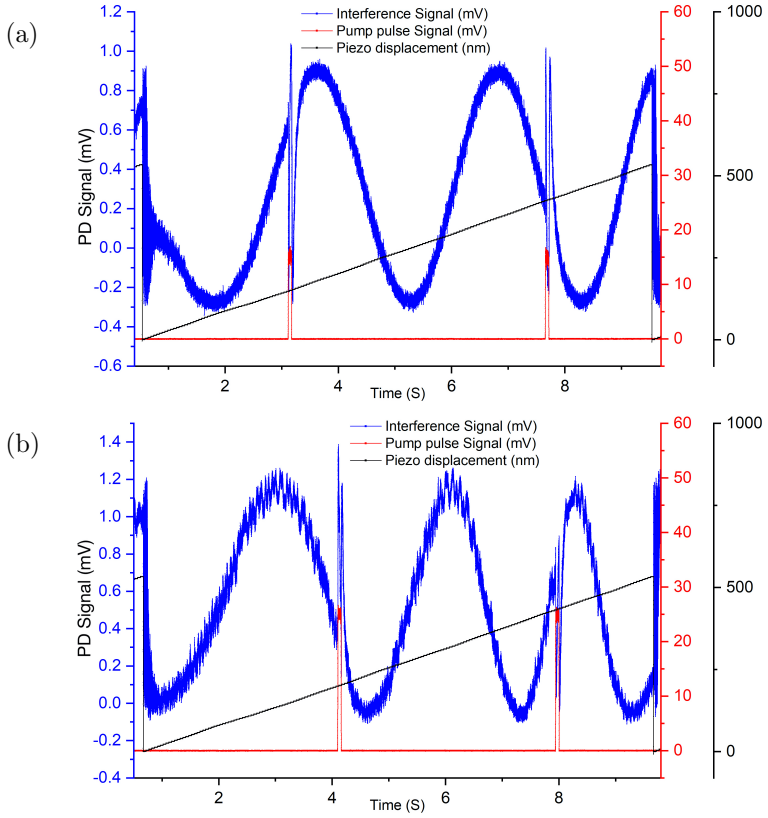

Figure 2.7: **Measuring single-point interference intensity against a reference displacement for calibration.** The interference signal (in blue) responding for the PZT assisted sample translation and also the pump laser effects (Pump signal in red). Sample reference movement in black corresponds to ramp voltage provided to the PZT. Pump laser power used: (a) 8.48 mW (b) 7.50 mW.

Fig. 2.7 shows the intensity recorded on an oscilloscope using PD1 at the centre of the obtained fringes (in units of mV). A ramp voltage ($0 - 20\ V$) was given to the piezo mount which has a calibration of translating around 26.6 nm in 1 V. The calculated displacement of the sample (silver wire) agrees with the input displacement. This calculation was based on the interference condition obtained from eq. (2.4), which implies that a half-fringe collapse or expansion (phase change of $\pi/2$) corresponds to a sample displacement (Δd) of $\lambda/4$ ($\approx 158\ nm$ in this case).

Also, to determine the direction of movement of sample upon pump exposure, two control pump pulses ($P = 8.48\ mW$) of 50 ms width each were imparted over the sample while it was being translated by the PZT mount in a known direction. The direction of translation of the PZT mount was already been calibrated (see Appendix B for the method used), making sure that upon getting a positive input ($0 - 20\ V$ in this case), the mount translates the sample in $(-z)$-direction. As seen in Fig. 2.7a, the first pulse creates a negative peak in the interference signal while it was in an increasing state and the second pulse creates a positive peak while the signal was in the decreasing state. This clearly indicates that the sample movement due to pump exposure is in the opposite direction (along $(+z)$-axis) of its uniform translation and is also counter-intuitively opposite to the direction of propagation of pump laser as it hits the sample. As a validation, a similar test (Fig. 2.7b) was performed with pump power changed to 7.51 mW which agreed with the previous observations. Therefore, as a convention, all further experiments were done with the pump pulse starting on the decreasing part of the signal, just to get an upward initial peak in the interference response.

2.3 Data acquisition and results

The optical setup shown in Fig. 2.1 was used to generate local perturbations in the two samples, silver mcro-wire ($\phi = 15\ \mu m$) and hair fibre ($\phi = 100\ \mu m$), using pump laser irradiation. The focused pump beam strikes at the centre of the sample, placed orthogonally to its direction of propagation. Another low-power laser propagating along the opposite direction as that of the pump beam, goes through an iLens interferometer setup and reflects off from the back of the sample to record its nano-mechanical dynamics in the form of an interferogram.

To capture the photo-induced interference dynamics of such micro-samples, firstly,

the central interference intensity before the pump light exposure is kept in the linear regime of its sinusoidal curve. This is done by carefully displacing the sample to scan through all the phases of the curve and then fixing it at the required position (this position corresponds to an interference intensity level as the one where the second pump pulse hits the sample in Fig. 2.7a). The initial direction of shift in intensity is also predetermined by moving the sample in a known direction and observing the change in signal, upwards or downwards. Now, pump pulse of varying power and widths are allowed to fall on the sample and their corresponding intensity variations are recorded.

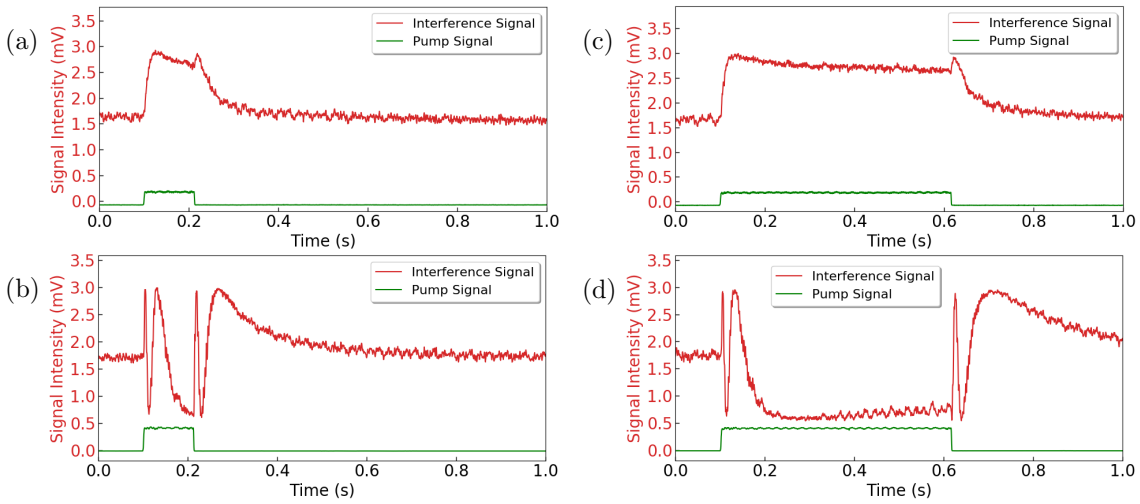

Figure 2.8: **Photo-induced interference dynamics of silver microwire.** Plots on the top and bottom results from $P = 0.53\ mW$ and $P = 2.21\ mW$ pump beam exposed for 100 ms (left) and for 500 ms (right). Corresponding pump signals are represented by the green curve underlying each plot.

Fig. 2.8 shows the interference intensity variation results obtained when the silver wire sample (Sample 1) undergoes photo-induced mechanical changes using a pump beam of power 0.53 mW and 2.21 mW, each of them exposed for a duration of 100 ms and 500 ms. The simultaneously recorded pump beam signal shows the pulse duration for which the sample is irradiated. Having a constant intensity initially when there is no pump exposure, the interference signal jumps off as soon as the pump pulse starts. Giving long enough time to the exposure, the signal saturates until the pulse is switched 'off'. Thereafter, the interference signal collapses back to its original value with a reduced rate. Higher power of pump laser resulted in more number of fringes crossed, caused by a farther central displacement of the sample in such cases. The exact magnitude of this displacement is calculated in Chapter. 3 using the phase

corresponding to each intensity point.

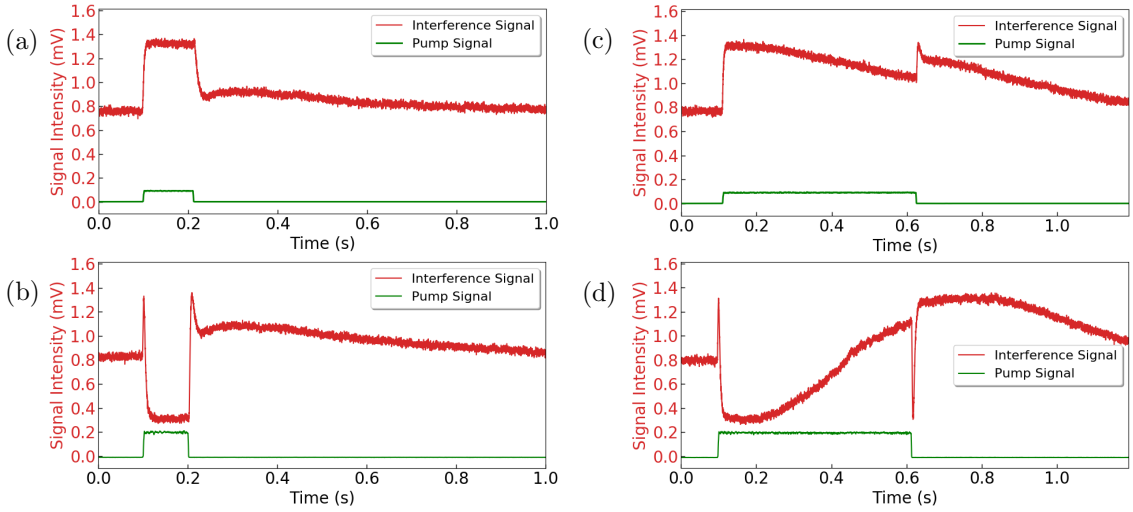

Figure 2.9: **Photo-induced interference dynamics of hair fibre.** Plots on the top and bottom results from $P = 3.24\ mW$ and $P = 9.42\ mW$ pump beam exposed for 100 ms (left) and for 500 ms (right). Corresponding pump signals are represented by the green curve underlying each plot.

Another dataset is acquired for hair fibre sample (Sample 2) exposed to pump laser of power 3.24 mW and 9.42 mW for same duration as with Sample 1. The results are shown in Fig. 2.9. Both the samples creates a near constant interference signal initially, but despite having lower irradiating power, the increment in signal from Sample 1 is greater than in Sample 2. This can be related to the fact that Sample 1 reflects a much larger proportion of pump light falling on it that results in a greater momentum transfer into it, creating a larger displacement. However, the rate of fringe movement, or the rate of displacement is higher for Sample 2 because of its property of absorbing the light energy faster than Sample 1. It in turn, also relaxes back to the original state faster than Sample 1. In both the cases, a full reversibility of the deformation or the displacement traversed is seen, since the pumping power used is in a low (mW) range. Higher powers ($> 40 - 50\ mW$) can easily damage the high absorbing sample like Sample 2 permanently.

To get better understanding of the dynamic motion of Sample 1 in relation to the exposure times, multiple interference intensity plots were acquired for a fixed pump power $P = 0.53\ mW$ and exposure time varied from 50 ms to 500 ms in steps of 50 ms. These plots are arranged as a stack and are aligned about the starting point of pump pulse as shown in Fig. 2.10. It is observed that the sample displacement attains

a maximum value at $\approx 200\ ms$ exposure time after which the intensity remains almost constant until the pulse ends. For exposure times greater than $200\ ms$, the signal just seems to remain saturated and stretches as per the pulse width.

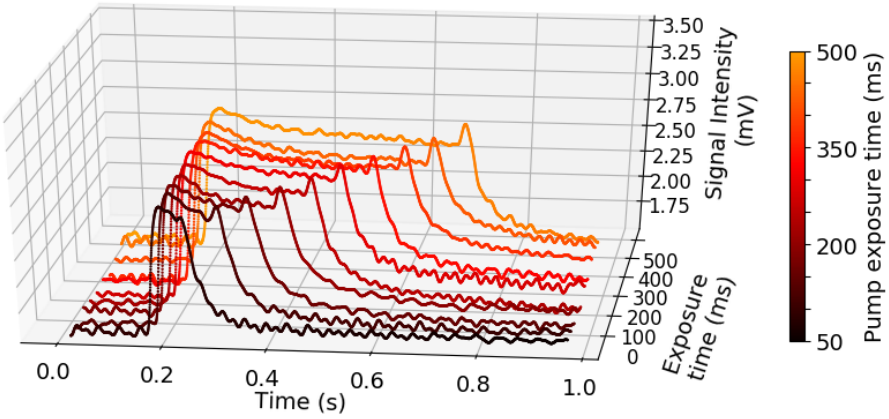

Figure 2.10: **Interference dynamics of silver microwire for a fixed pump power and varying exposure times.** Plots in increasing order of pump exposure time (shown along the in-plane axis) from 50 ms to 500 ms in steps of 50 ms. Pump power was fixed at $P = 0.53\ mW$.

For most of the plots in Fig. 2.10, the interference from sample undergoes about a quarter fringe expansion which can be roughly estimated as a result of $\lambda/8 = 79\ nm$ displacement of the central region of the sample. But to create a definite distinction within these close observations, a point-by-point displacement conversion is required to obtain their corresponding displacement vs. time plots. A detailed discussion on development of such a conversion process is covered in Chapter 3. The results obtained when applying the conversion for the data from this chapter are shown towards its end which serves a better explanation of the dynamics and helps in understanding of the motion of these microscale systems.

Chapter 3

Displacement extraction from homodyne interference system

The wide use of optical interferometry-based techniques to perform non-contact dynamic measurements has put severe demands on development of the interferometric methods used in them. Processing and analysing the output optical signal is an indispensable part of these techniques, which are aimed at measuring the optical path-length change of the source light which emerges as a result of motion, deformation, or uneven surface features of an object [27]. Techniques developed under Interferometric dynamic measurement (IDM) as reviewed by Yu Fu et al. in [28], falls under two main types; one that are based on two-dimensional camera based detectors and other using single-pixel photodetectors. Camera based detection techniques uses sensors like CCD or CMOS to capture a full-field measurement of fringe patterns at a high frame-rate to convert into the desired information by expert interpretation. On the other hand, single-pixel IDM offers point-wise measurement with a much higher temporal resolution, but its limited range in spatial domain makes it less appealing for applications that require area sampling of objects for accurate mapping of multiple physical quantities related to it.

Two typical interferometric configurations that uses single-pixel detection technique are the heterodyne Mach-Zehnder interferometer and the homodyne Michelson interferometer. The one used for the study presented in this thesis is derived from the latter. It takes central measurement point on the fringe pattern falling on the detector to record the time varying interferometric intensity at that point. Sampling rate of the detector is 2500 measurements/s, which satisfies the Nyquist sampling theorem since the sample's movement in the experiment is typically several millimetres per second. The interferometric signal is then altered to reduce its noise and processed using phase

extraction algorithms and a sequence pulse counting method which completes its conversion into a displacement variation along the time axis.

This chapter begins with formulating a general expression that relates each step displacement with the intensity change calculated in Section 2.2, at the point of detection. The same equation is used to generate a computational simulator of the experiment that assumes the sample displacement of an exponential form to provide its corresponding self-generated intensity signal. Two phase extraction algorithms are then developed and applied over a common test signal simulated for some fixed experimental parameters which compares them over their respective errors. The most efficient method is then used to convert results from Chapter 2 into corresponding displacement plots that represent the dynamics of micro-samples and helps in analysing their temporal intensity variations resulting from the changing experimental parameters.

3.1 Theoretical and computational studies of the interferometric signal

In Section 2.2, theoretical calculations for the interferometric system resulted in Eq. (2.4), which relates the interference intensity to the sample displacement with time. To generate measurements from the interference intensity signal obtained from the experiments, this equation is analysed and transformed to provide a theoretical ground for the numerical computation that helps in extracting sample's displacement. This section formulates the required signal transformation for use in computational algorithms and later discusses over an experimental simulator that can help in developing these algorithms in many ways.

3.1.1 Signal formalism

Eq. (2.4) representing central fringe intensity in terms of sample displacement is given as,

$$I(x_0, y_0) = 4I_0 \cos^2(kz(t)) \tag{3.1}$$

where $k = 2\pi/\lambda$, λ being the wavelength of the interfering light and $z(t) \equiv \Delta d(t)$ is the sample displacement, assuming $\Delta d(0) = 0$.

Although, Eq. (3.1) alone can be directly used to get a very rough estimate of the displacement $z(t)$, based on the fact that a phase change of $\pi/2$ in the $\cos^2$ argument results in a maxima to minima transition of interference intensity (I) and using a fringe counting technique as mentioned in Section 3.2.1, but to obtain an ultra-precise displacement, each step intensity recorded in the detector signal has to be converted correspondingly. For this, we first take Eq. (3.1) into consideration and denoting the maximum intensity amplitude $4I_0$ by a single term I_0 for simplicity, we get,

$$I(z) = I_0 \cos^2(kz)$$

However, a more practical form of the intensity signal that we actually observe through the detectors, taking background noises and random constant phase difference into account is,

$$I(z) = I_b + I_0 \cos^2\left(\frac{\beta z - \delta}{2}\right) \tag{3.2}$$

or,
$$I(z) = I_b + \frac{I_0}{2}\left(1 + \cos(\beta z - \delta)\right) \tag{3.3}$$

where, I_b = Background signal intensity,

$\beta = 4\pi/\lambda$

Also, $\delta = n\pi$, $n \in R$, is the initial phase difference between the two interfering waves. Rewriting Eq. (3.3),

$$I - I_b = I^{'} = \frac{I_0}{2}\left(1 + \cos(\beta z - \delta)\right)$$

$$\left(\frac{2I^{'}}{I_0} - 1\right)^2 = \cos^2(\beta z - \delta)$$

$$\sin(\beta z - \delta) = \frac{2}{I_0}\left(I^{'}(I_0 - I^{'})\right)^{\frac{1}{2}} \tag{3.4}$$

Differentiating both sides of Eq. (3.3), we get:

$$dI = -\frac{\beta I_0}{2}\sin(\beta z - \delta)dz$$

$$dI = -\frac{\beta I_0}{2}.\frac{2}{I_0}(I^{'}(I_0 - I^{'}))^{\frac{1}{2}}dz \qquad \text{(using Eq. (3.4))}$$

or,
$$dz = \frac{dI}{-\beta\sqrt{(I - I_b)(I_0 - (I - I_b))}} \tag{3.5}$$

Each small displacement from the resulting relation in Eq. (3.5) can be cumulated over time axis to obtain the required sample displacement.

3.1.2 Computational simulations

Computational techniques are adopted to numerically calculate the interference intensity under a presumed form of sample's motion. Without bothering about pump light and its power, both the rising part (pump 'on') and the falling part (pump 'off') of the displacement are presumed to follow an exponential curve. A simulated interference intensity is thus obtained using Eq. (3.2), which is completely controllable and customisable in terms of various experimental parameters such as displacement amplitude, pump exposure duration, initial phase difference and other factors that determines the shape of the exponential displacement parts. Following is the formation of equation set for the displacement function to be used in the simulator program.

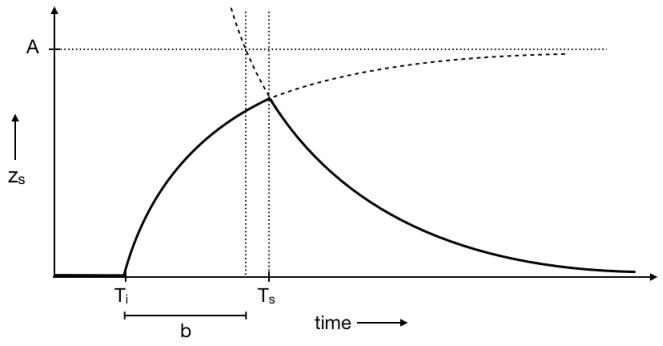

Figure 3.1: **Simulated displacement function.** Displacement function corresponding to Eq. (3.6) having exponential forms for both of its major sections.

The simulated displacement function ($z_s(t)$) is assumed as,

$$z_s(t) = \begin{cases} 0 & t < T_i \\ A\left(1 - e^{-\frac{t-T_i}{T_1}}\right) & T_i \leq t \leq (T_i + T_s) \\ Ae^{-\frac{t-T_i-b}{T_2}} & t > (T_i + T_s) \end{cases} \tag{3.6}$$

where,

$$A = \text{Displacement amplitude } (nm)$$

$$T_1 = \text{Time constant for rising equation } (sec)$$

$$T_2 = \text{Time constant for falling equation } (sec)$$

$$T_i = \text{Shutter start time } (sec)$$

$$T_s = \text{Shutter duration } (sec)$$

and b is the time shift needed to be introduced in the final part of the displacement function $z_s(t)$, to keep it continuous at time T_s.

So, in order to keep $z(t)$ continuous at $t = T_s$ (assuming $T_i = 0$ for simplicity),

$$\begin{aligned} Ae^{-\frac{T_s - b}{T_2}} &= A\left(1 - e^{-\frac{T_s}{T_1}}\right) \\ -\frac{T_s - b}{T_2} &= ln\left(1 - e^{-\frac{T_s}{T_1}}\right) \\ b &= T_s + T_2\ ln\left(1 - e^{-\frac{T_s}{T_1}}\right) \end{aligned} \tag{3.7}$$

Now, using Eq. (3.6) and (3.7) in Eq. (3.2) to get the simulated signal Intensity $I_s(t)$ as an implicit function of t as,

$$I_s(t) = I_b + I_0 \cos^2\left(\frac{\beta z_s(t) - \delta}{2}\right) \tag{3.8}$$

Based on the displacement function (z_s), a simulator program was developed that generates a corresponding central intensity function using Eq. (3.8) as shown in Fig. 3.2. It is equipped with five adjustable parameter sliders to recreate a range of possible experimental scenarios.

In addition to creating an intensity signal of a similar form as observed practically, to achieve a better imitation of the experiment, the simulator program also adds a noise to the signal which is essentially an array of randomly picked values from a gaussian, averaged at 0. The signal thus generated could be used as a benchmark for the displacement conversion algorithms discussed in later sections of this chapter and would provide a variety of tests for them to run.

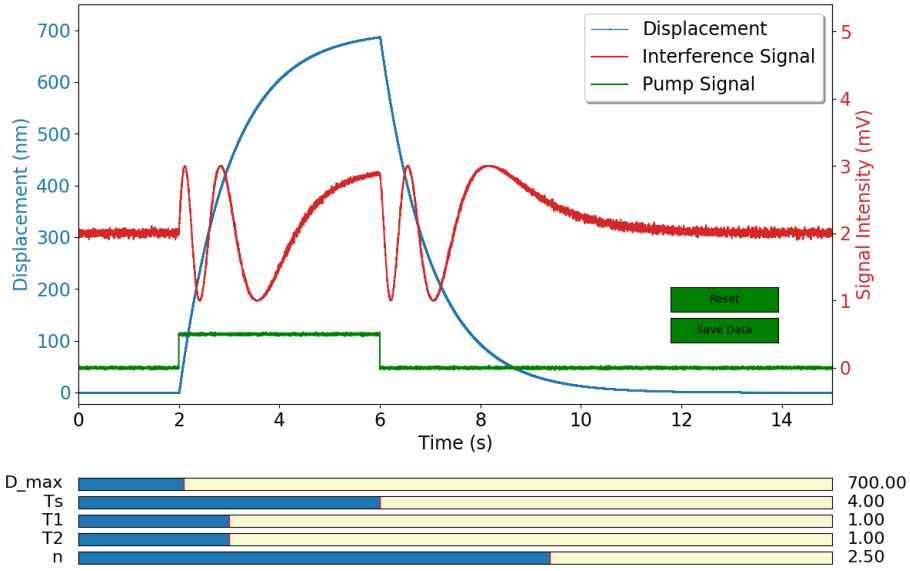

Figure 3.2: **Experimental simulator generating interference signal and pump signal from a given sample displacement function.** Interference signal (in red) has taken its form in accordance with five arbitrarily valued experimental parameters represented by five adjustable bars under the graphs. Their current values are shown on the right.

3.2 Algorithms for displacement conversion

Theoretical basis of interference intensity discussed in previous section paves the way for development of computer programs that converts the Intensity vs. Time signal recorded in the experiment to Displacement vs. Time, and thus helps in quantitative representation of sample's microscale dynamics. These programs are made using Python and require the pre-collected interference dataset as input to convert according to their underlying algorithms into displacement data as output, where everything takes place after the actual physical experiment has already been completed.

Two main methods are used here to generate data about relative displacements from the interference phenomena, which forms two algorithms, Algorithm 1 and Algorithms 2. In first method, peaks counting technique and linear signal transformation is used to compute the displacement, which is fast but gives a very low resolution output. Whereas, second method digs further deeper within consecutive peaks and uses a sinusoidal transformation, resulting in ultra-high resolution conversion which is however a bit slower. This section describes the development of the two algorithms which also makes use of a common test-data generated using the experimental simulator described in Section 3.1 for test-runs and error analysis.

3.2.1 Linear sequence algorithm

Under this method, the change in the signal intensity at the detector as it moves from trough to peak is recorded. This change corresponds to a displacement of one-fourth of the wavelength of light source ($\lambda/4$), and by counting the number of maximas (peaks) and minimas (troughs) the total displacement can be calculated. The resolution of this measurement is therefore 158 nm, or fourth of the wavelength of a He-Ne laser. This type of measurement technique combined with a little tweaking by heterodyning the frequency of laser can be used to produce higher resolution industry grade interferometers.

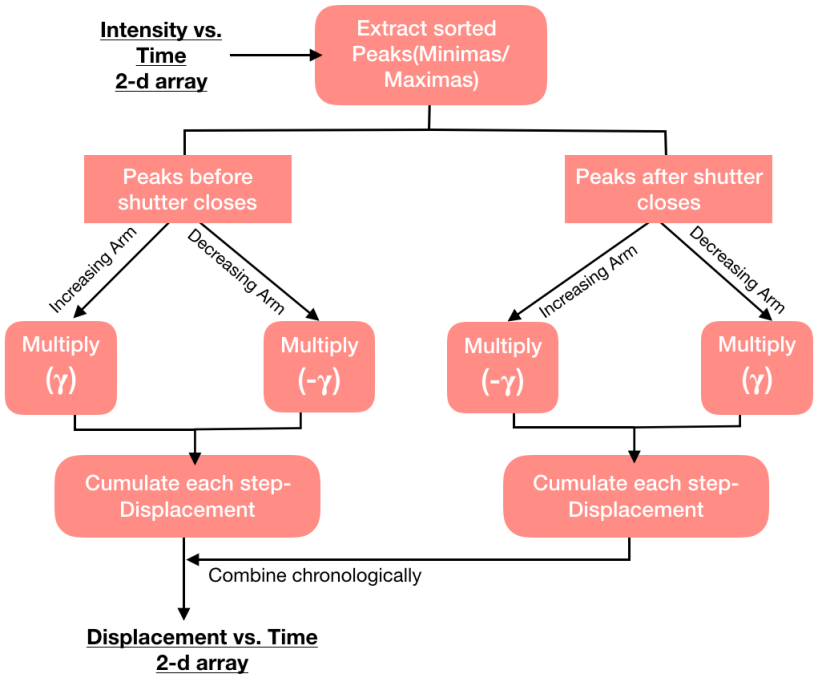

Figure 3.3: **Working flowchart of Linear sequence algorithm**

Stepwise flow of the Linear sequence algorithm (Algorithm 1) is shown in Fig. 3.3. It takes the two-dimensional Intensity-Time array and extracts its sinusoidal peak and trough points. For the points falling before the time when pump pulse ends (when the shutter closes), their count number is multiplied with the conversion factor (γ) which is subtracted or added to previous displacement value according to the state of signal, peak to trough (decreasing state) or trough to peak (increasing state). Inverse of this is applied to the points falling after the pulse ends, since the direction of displacement becomes opposite in this case. And thus, both are combined to give the output displacement.

The conversion factor (γ) mentioned above relates the displacement step to the

intensity step as $z_{\Delta I} = \gamma(\Delta I)$, where (ΔI) is the change in intensity. And according to Eq. (3.2), $z = \pi/\beta = \lambda/4$ corresponds to a half-fringe collapse (peak to trough or trough to peak) for intensity amplitude (I_0), therefore, the conversion factor becomes $\gamma = \lambda/(4I_0)$ for change in intensity of $\Delta I = I_0$.

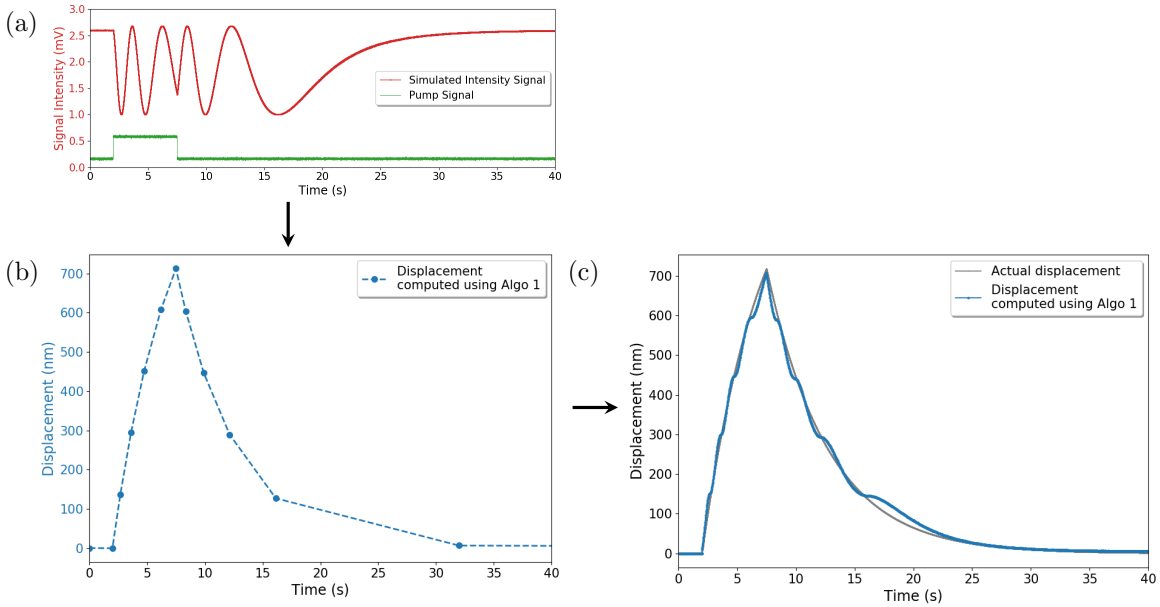

Figure 3.4: **Displacement conversion using Linear sequence algorithm.** (a) Simulated interference signal, used as the data for testing the algorithm. (b) Intermediate step of conversion. (c) Extracted displacement (blue) and the actual displacement (grey) together shows the poor accuracy of this algorithm at non-extreme points of input signal.

Algorithm 1 is tested using a simulated signal shown in Fig. 3.4a. Following are the parameters set in the simulator to generate it:

$$\text{Maximum displacement } (D_max) = 718.0\ nm$$

$$\text{Total time} = 40\ sec$$

$$\text{Pulse width } (T_s) = 5.5\ sec$$

$$T_1 = 5.2\ sec$$

$$T_2 = 5.2\ sec$$

$$\text{Pulse start time } (T_i) = 2.0\ sec$$

Peaks and troughs identification and their corresponding displacement markers (Fig. 3.4b) works as an intermediate step for the working of Algorithm 1. Complete conversion result is shown in Fig. 3.4c, which is overlapped with the simulated (actual)

displacement curve. It can thereby easily be seen that linear conversion is accurate only upto a resolution of $\lambda/4$ and using the same linear multiplication factor for the data points within this limit results in an error. This is clear from the large wavy deviations from the actual curve observed in the output. However, the error in determining the maximum displacement amplitude is not as high. The output displacement peaked at 707.63 nm, showing an error of 1.44% from the actual value (D_{max} = 718.00 nm). Thus, a transformation based on the functional form of the interference signal is required to eliminate the errors at the deepest levels, which is discussed in the following improved algorithm.

3.2.2 Differential algorithm

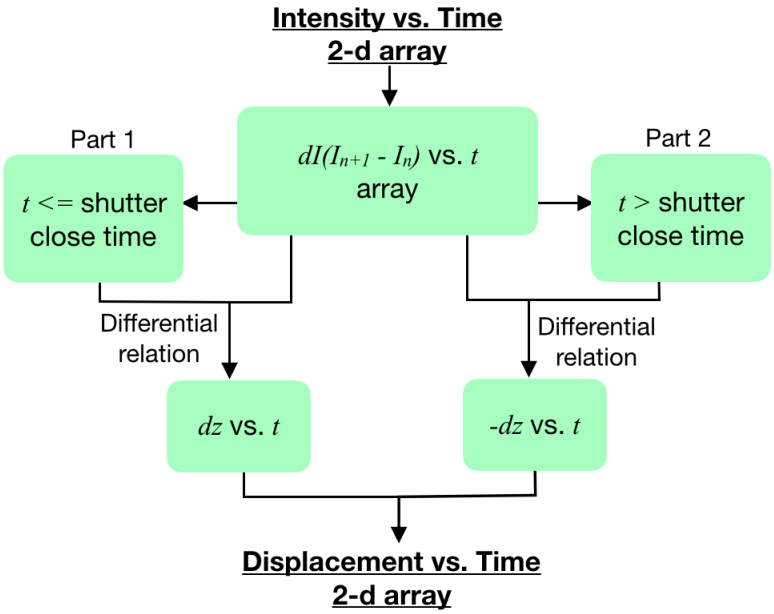

Figure 3.5: **Working flowchart of Differential algorithm**

This algorithm is based on a functional transformation method that uses phase extraction algorithm at each signal point and converts it into the point displacement using Eq. (3.5), and thus integrating each of these small displacements along whole time domain gives the complete output. The intensity curve is a sinusoidal function, and as long as the displacement jumps between measurement points do not exceed $\lambda/4$, they can be computed from the sinusoidal transformation. A sensing system using this method, theoretically has an infinite resolution. However, in practice, the precision and sampling rate of the detection devices used and the signal to noise ratio (S/N ratio) limits the resolution, although sub-nanometer resolution can easily be

achieved as detailed in Section 3.3 of this thesis.

Stepwise flow of the working of differential algorithm (Algorithm 2) is shown in Fig. 3.5. From the two-dimensional Intensity vs. Time array, each consecutive signal point pair is extracted and bifurcated based upon their time of occurrence. For points before the pump pulse ends, the transformed small displacement (dz), calculated using the differential relation $dz = dI/(-\beta)\sqrt{(I - I_b)(I_0 - (I - I_b))}$ from Eq. (3.5), is added to the previous displacement and for the pairs after the pump pulse ends, they are subtracted from the previous displacement. This iteratively applies along the whole time axis to obtain the final Displacement vs. Time array.

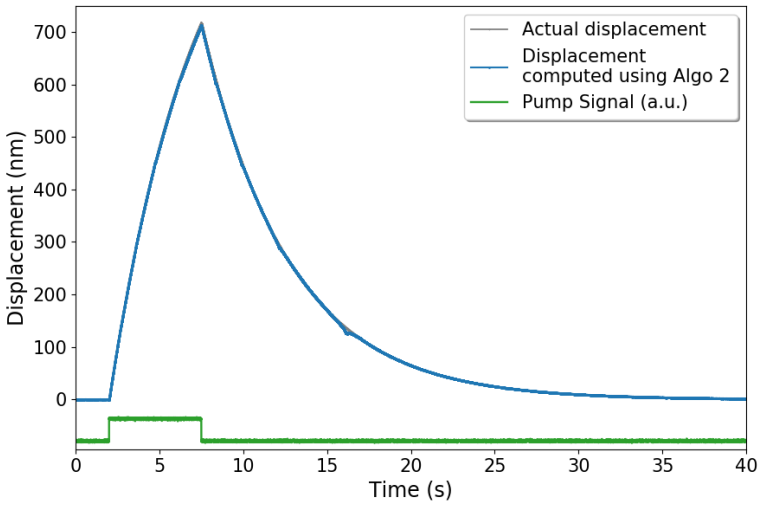

Figure 3.6: **Displacement conversion using differential algorithm.** Extracted displacement (blue) and the actual displacement (grey) used for signal simulation, shows a near complete overlap.

Program based on Algorithm 2 is tested over the same simulated signal (Fig. 3.4a) as used with Algorithm 1. Fig. 3.6 shows the conversion results where the output is matching closely with the actual plot. This is a consequence of point-by-point signal transformation using the sinusoidal form of the input interference intensity to accurately measure each step displacement. In addition to eradicating the huge error that was observed with the previous algorithm in the form of the wavy displacement output, this also shows a reduction in the error in determining the maximum displacement amplitude. It is 716.18 nm as observed in this case, which corresponds to an error of 0.25% from the actual value (D_{max}=718 nm). However, there are still minute deviations in the extracted displacement at the points of interference signal maximas and minimas. This can be made clear by looking at its residual error plot, as shown in Fig. 3.7.

The figure shows the residual error of the displacement calculated using Algorithm 2 and also includes the one from Algorithm 1. The error of the former at the point of maximum deviation is $-12.91\ nm$ (1.79% error). This is much less as compared to the latter, whose is $-39.31\ nm$ (5.47% error). The limited flaws in Algorithm 2 are in the form of small kinks both positive and negative, caused by the the fact that the value of the differential displacement element dz becomes close to a singularity at the points where the value of $(I - I_b)$ approaches I_0 according to Eq. (3.5). This sort of error is almost inevitable unless an infinitely small intensity step (dI) is used, which is practically impossible in numerical computations.

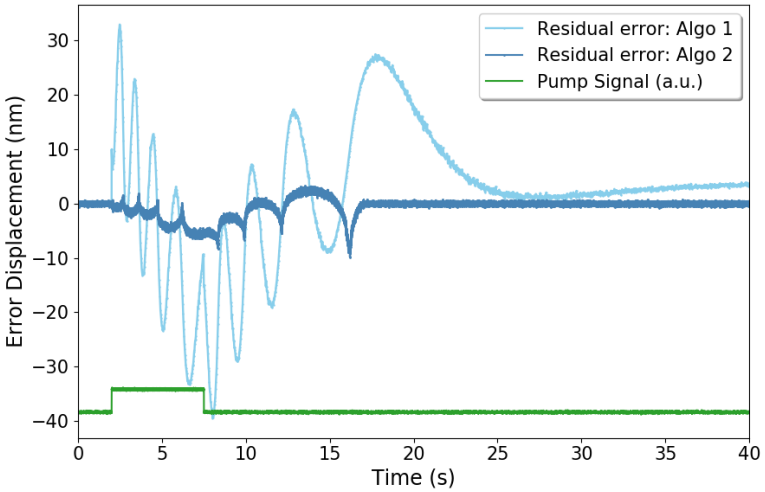

Figure 3.7: **Residual errors in calculated displacements for the two algorithms.** Error corresponding to Algorithm 1 is in light blue and of Algorithm 2 is in dark blue. The latter shows a reduced error with peaks at interference extremums.

Conclusively, the more accurate Differential algorithm is thereby used for converting the interference data recorded by the system in further experiments to analyse sample dynamics.

3.3 Results and analysis

Experimental results of generating local perturbations in silver wire sample ($\phi = 15\ \mu m$) using pump laser irradiation have been discussed previously in Section 2.3. There we were able to observe the interferometric intensity variations when the sample underwent a series of varying pump exposures. Now, the displacement of the sample in that experiment is extracted using the differential algorithm. Results of which are

shown in Fig. 3.8.

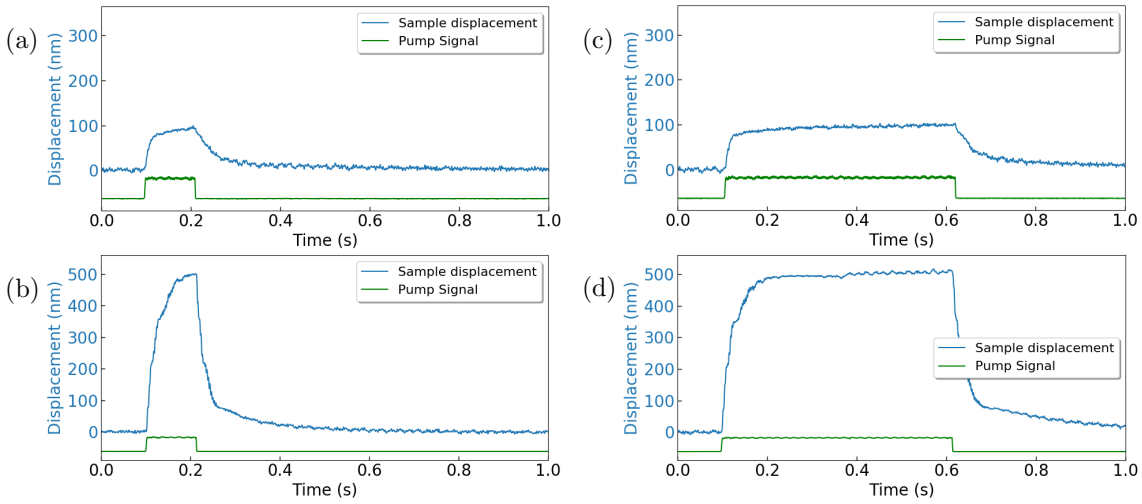

Figure 3.8: **Photo-induced dynamical response of silver microwire.** Plots showing the dynamical displacements (blue) of sample on top and bottom resulting from $P = 0.53\ mW$ and $P = 2.21\ mW$ pump beam exposed for 100 ms (left) and for 500 ms (right). Corresponding pump signals are represented by the green curve underlying each plot.

A maximum displacement of 99.23 nm and 103.30 nm was observed for the cases with pump power $P = 0.53\ mW$ and exposure time of 100 ms and 500 ms respectively. Whereas, the maximum displacement observed for the cases with pump power $P = 2.21\ mW$ and similar exposure times was 500.39 nm and 516.29 nm respectively. This shows a higher peak movement of the sample on exposure of higher power of pump light. But, to also get a similar conclusion about the relation of peak displacement with exposure times, another set of interference data was analysed whose extracted displacements are stacked together as shown in Fig. 3.9. Here, multiple experiments were performed for a fixed pump power ($P = 0.53\ mW$) and exposure time varying from 50 ms to 500 ms in steps of 50 ms. Previously obtained interference intensity signals corresponding to this data-set can be referred from Fig. 2.10.

As observed previously in Section 2.3, the peak sample displacement attains a maximum value for around 200 ms exposure time and remains not much deviated from this value until the exposure ends, these results also follow the same pattern. However, here this can be explicitly measured and compared since the dynamics of sample movement are readily available. Initially, before pump exposure starts, a constant zero displacement is observed. Simultaneously recording the pump exposure and the interference signal resulted in a synchronous displacement rise at $t_i = 0.1\ s$ as seen in Fig. 3.9. This exposure lasted for varying times, where a stable maximum

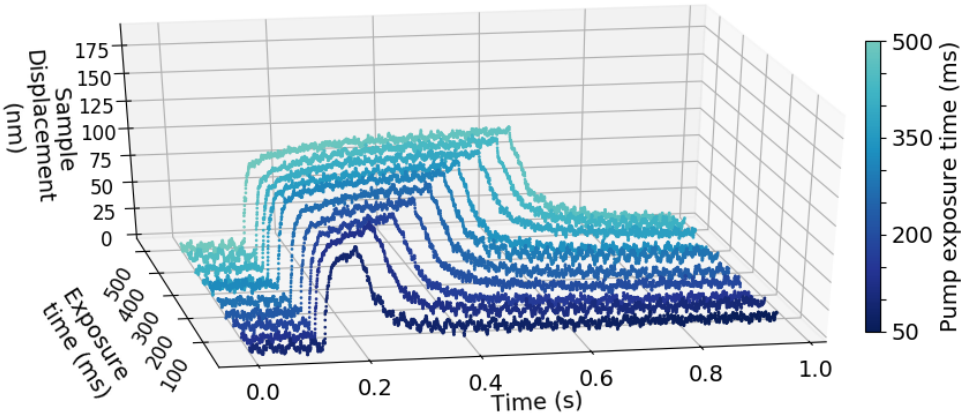

Figure 3.9: **Photo-induced dynamical response of silver microwire for a fixed pump power and varying exposure times.** Plots in increasing order of pump exposure time (shown along the in-plane axis) from 50 ms to 500 ms in steps of 50 ms. Pump power was fixed at $P = 0.53\ mW$.

displacement point is achieved in most of the cases with long enough exposures. After the exposure ends, the fall in displacement experienced by the sample follows a similar form in each case, thereby showing no sign of deformation effects in any case. This is because of the low irradiance power used. Also, attributing the central shift of the sample to a consequence of the generation of thermal strain inside its body can explain this stable top plateau as attainment of thermal equilibrium. In this state, the extra energy absorbed by the sample other than what is causing it to displace, is equal to the energy radiated from its surface into the surrounding atmosphere. In this way, our interferometer system with its fringe analysis technique is capable of studying micro-mechanical disturbances in small samples when perturbed using low-powered light radiations.

Chapter 4

Further extensions for other measurables

For an experimental system to be capable of performing high precision surface metrology and dynamical tracking of microscale systems, it is of utmost importance to have the ability to rapidly obtain nanometer-resolved spatial information. However, these may not always be the only physical quantities that can be measured using such system abilities. There are other measurable quantities that can be analysed about the microscale systems which requires a little tweaking or making small changes in the current experimental setup.

As the title of this chapter suggests, it covers a method using the experimental basis of the previously used setup of iLens interferometric probing, having undergone specific modifications that allows it to further extend the scope of this idea to measure physical properties that specifically explains and are sometimes unique for microscale systems. Although these properties are not thoroughly studied upon in this thesis, this chapter tries to describe the extensibility of the original interferometric system as an initial milestone towards exploring such aspects of microscale systems.

4.1 Mechanical response delay measurements

Investigating a number of physical properties and force effects on microscale objects require scaling of such forces to fit into the system dimensions. However, these forces are not often the only things that are needed to be taken care of. Another important parameter to consider in some cases is the response time. The response time for mechanical systems and its scaling is briefly discussed in Chapter 1.1.

In this section, a slight experimental modification in the previously used iLens based interferometer setup is proposed that allows it to measure the response delay in the dynamic effects shown by a hair fibre sample on pump light irradiance. It should be noted that the measurement results from this experiment are of the response delay observed and not the actual response time of the sample, since there are other factors like delay in the detection system that sums up with the actual response time to give a combined delay in observing the effects of pump irradiance. These measurements are taken for both the situations when the pump exposure starts rising the displacement and when it ends, causing a sudden fall in displacement of the sample.

4.1.1 Experiment

The setup for this experiment uses the movable mirror which reflects the focused pump light on the sample (see Fig. 2.1 for reference). This mirror is made to shift the focal spot of pump laser over the length of the sample (along x-axis) to irradiate other parts of the sample rather than just the centre. Total length of the sample is 15 mm and there are seven points of exposure set over the sample's length at 3 mm, 5 mm and 7 mm on one side of the centre and at similar spacing on its other side, as shown in Fig. 4.1a. In each of these cases, interferometric probing is done on the centre part of sample as usual.

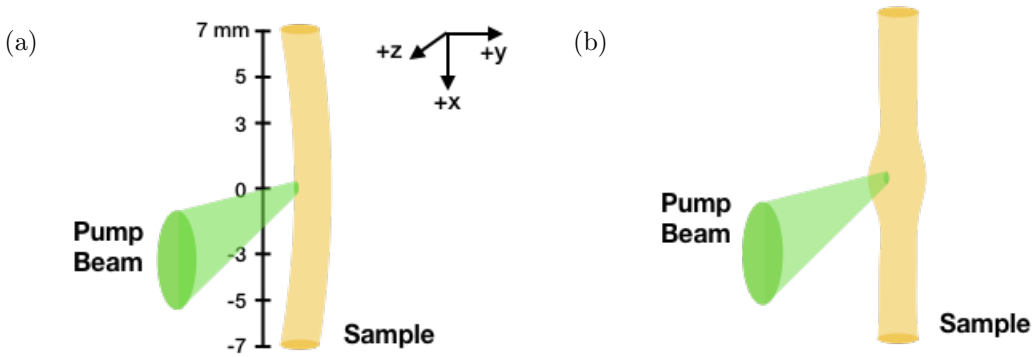

Figure 4.1: **Effects of focused pump laser irradiance on hair fibre.** (a) Bending of the sample at the point of exposure with other exposure points marked on its side for the response delay measurement experiment. (b) Bulging of sample at the point of exposure, usually caused by its over heating as a result of using high power pump light.

Response timings for both situations when the pump light hits the sample (displacement rise) and when it turns off (displacement fall) were extracted using the difference

in times of the interference signal change and pump signal change. Suitable conventions were followed for selecting the particular time of change in a signal throughout the observations. Each of the seven points of response delay measurements were repeated for four different pump powers ($P = 0.5,\ 1.0,\ 5.0$ and $10.0\ mW$) to observe the effects of change in irradiance power on the response delay.

4.1.2 Results

Results of the observed response delay in hair fibre sample during the rising displacement or pump-on states are shown in Fig. 4.2. It shows an overall decrement in response delay on increasing the pump power. Also, the result of response delay during the falling displacement or pump-off states are shown in Fig. 4.3. Many of the cases in both the situations show a central local peak and also some sort of symmetry around it, depicting the similarity in response of the sample at same distances about its centre. Moreover, these observations are more common in particularly pump-on responses because the sample responds from a more stable state in this situation than in pump-off responses where it changes from an already dynamic state. As a result, the average response delay for rising displacement is 1.96 ms whereas, it is 0.81 ms for falling displacement.

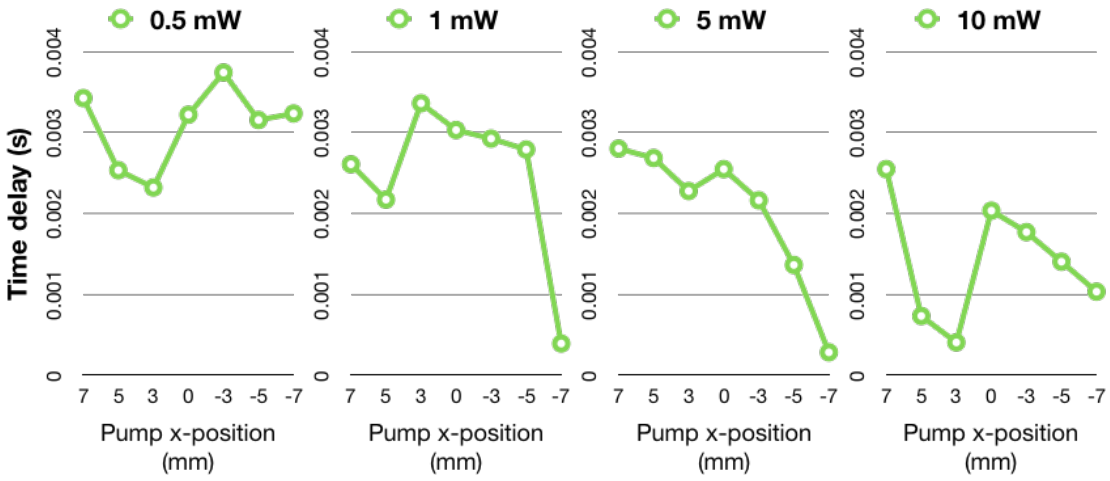

Figure 4.2: **Response delay observed in hair fibre during displacement rise.** Plots from left to right corresponds to increasing pump power from 0.5 mW to 10.0 mW with each plot having the pump exposure position on x-axis.

Above mentioned observations indicates the pump-on response being more reliable in measuring the response time of microscale samples using this method. Also, it should

be noted that a response delay of about 2 ms on average is very close to the time taken by the pump signal to reach from zero to its maximum as the shutter blocking the laser path is opened. This makes the response delay observations more erroneous and require a faster pulse transition technique that has a better open and close time than the current mechanical shutter.

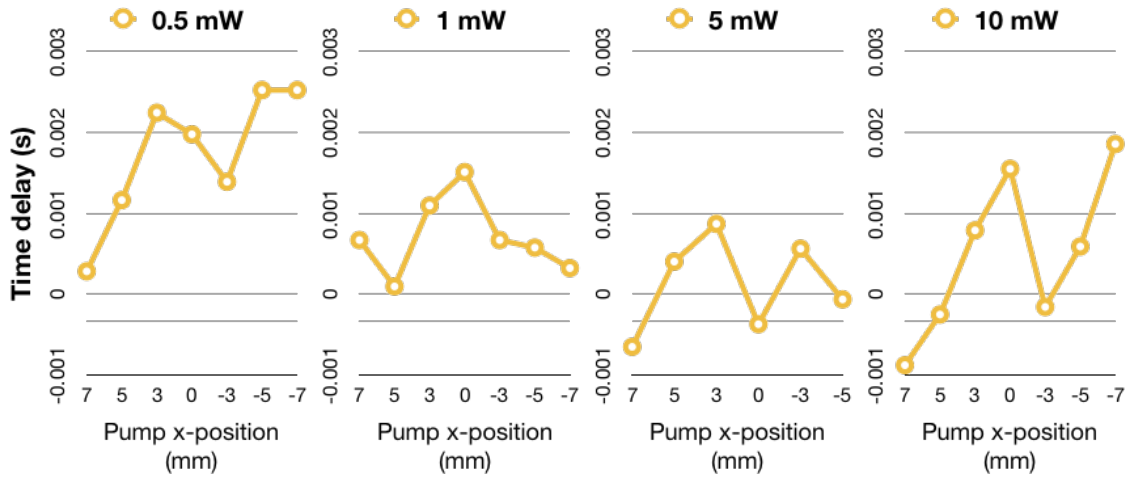

Figure 4.3: **Response delay observed in hair fibre during displacement fall.** Plots from left to right corresponds to increasing pump power from 0.5 mW to 10.0 mW with each plot having the pump exposure position on x-axis.

Conclusively, the experiments described in this thesis were successful in performing the task they were designed for, upto a level which can further be scaled up to achieve more accuracy and reliability in their measurements. With a faster technique to create pump pulses, the response delay measuring experiment can improve on the randomness in its current observations. These experiments thus holds great possibilities for extending the research work described in this thesis.

Chapter 5

Conclusions

5.1 Contributions of this thesis

In this thesis, an experimental method is presented for optically probing thermo-mechanical strain in fibre-like microscale systems. We demonstrated its working on a thin silver wire and a human scalp-hair fibre specimen. While focused laser beams are used to irradiate these specimens, central technique to the complete experimental system is the iLens interferometer. Studies of temporal profile of dynamic interference fringes are carried out using the superposition principle of light waves. Theoretical and computational analysis of the interferometric fringes led to the development of convenient computer programs to extract explicit dynamical information out of the system. Further modifications in the interferometric probing system are introduced to enable the study of additional physical properties of the microscale systems, like response time etc. The key features of this thesis are:-

- Nano-meter resolved experimental measurements of thermo-mechanical dynamics of microscale systems.
- A simulator for the experiment to generate test signals and study the experimental phenomena in greater detail.
- A computational program to extract dynamical information from a homodyne optical interference system.
- Response time measurements of microscale objects.

The general methodology employed for above mentioned techniques consisted of beginning with an experimental model that aims at measuring the required physical quantities of a subject system. This is used to form the optical setup, followed by a

theoretical or computational analysis of the underlying phenomena. Then the experiments are performed using suitable parameters that are able to exploit the physical phenomena to be measured efficiently on the given material specimens. The observed experimental data is processed and analysed to get the desired results.

Chapter 2 handles the experimental development of the interferometric system to measure the nanometer resolved dynamics of observed samples. A laser beam with a probing head of 8 μm in size strikes the surface of sample having width as low as 15 μm. Resulting interference intensity at the centre of the fringe pattern formed is recorded by the detection system. Linear sequence algorithm developed in Chapter 3 converts the intensity signal into sample displacement, with an error of 1.44% in calculating the maximum displacement experienced by the sample. This algorithm is replaced by a more accurate algorithm showing 0.25% error for this measurement. The former algorithm used linear conversion technique based on the fact that a peak to trough transition (or half-fringe collapse) of the sinusoidal interference intensity signal results from a displacement of $\lambda/4 \approx 158\ nm$. This technique fails to work for the signal points falling between consecutive peaks and troughs, therefore it is found to suffer a maximum deviation of 39.31 nm from the actual simulated displacement (having 718 nm peak value) while testing. On the other hand, the latter, differential algorithm suffers less error, with a maximum deviation of 12.9 nm. Also, a technique is discussed in Chapter 5 that is used to measure the response time of a 14 mm long hair fibre sample. Its results showed that the sample takes an average delay of 1.96 ms in responding for a focused light exposure turned 'on', and an average delay of 0.81 ms in responding for it after it turns 'off'.

5.2 Future scopes

Techniques in optical metrology have been using interferometry as an indispensable tool to carry out the most sensitive measurements with extraordinary precision and speed. Is is widely used for measuring small displacements and surface features in the fields of science and engineering. Being a non-contact method for probing sample surfaces, it uses a variety of phase change quantification techniques to achieve a sub-nanometer level resolution in measurements. Phase-shifting interferometry (PSI) and Vertical-scanning interferometry (VSI) are the techniques derived from it that specifically helps in getting improved resolution and larger dynamic range. Programs developed in this thesis enables increased rate of repetitive interferometric measurements and the ability to track the dynamics of microscale samples, like even the light-absorbing hair fibre,

with such an ease that it allows for its further applications in dynamical measurements of smaller organic samples.

Some of the possibilities for extending the research work described in this thesis could include improvising the response time measurement technique of microscale systems by using a pumping source that allows a faster pump pulse switching. It is also possible to carry out two-dimensional dynamical tracking of thin micro-fibres by using another iLens probe, orthogonal to the current one in the lateral plane. Specifically focusing on the samples with a fibre-like shape because of their rotational symmetry, this method could facilitate an experimental system capable of capturing two-dimensional dynamics of such samples.

Appendix A

Calculating the total interference intensity

The total interference intensity ($I(x,y)$) is square of the net field given by the summation of electric fields representing the reference beam ($\vec{E}_R$) and the sample beam ($\vec{E}_S$), which are:-

$$\vec{E}_R = E_{R_0} e^{i\theta_1} \qquad \text{using Eq. (2.2)}$$

$$\vec{E}_S = E_{S_0} e^{i\theta_2} \qquad \text{using Eq. (2.3)}$$

where, $\theta_1 = kz_1 - \omega t$ and $\theta_2 = kz_2 - \omega t + \xi(x,y)$.
We have,

$$\begin{aligned}\vec{E}_{net} &= \vec{E}_R + \vec{E}_S \\ &= E_{R_0} e^{i\theta_1} + E_{S_0} e^{i\theta_2} \\ &= E_{R_0}(\cos\theta_1 + i\sin\theta_1) + E_{S_0}(\cos\theta_2 + i\sin\theta_2)\end{aligned}$$

$$\therefore \qquad \vec{E}_{net} = (E_{r_0}\cos\theta_1 + E_{s_0}\cos\theta_2) + i(E_{r_0}\sin\theta_1 + E_{s_0}\sin\theta_2)$$

now since $I(x,y) = \left|\vec{E}_{net}\right|^2 = \vec{E}_{net} \,.\, \vec{E}^{\star}_{net}$, where $\vec{E}^{\star}_{net}$ is the complex conjugate of $\vec{E}_{net}$, we can substitute as,

$$\begin{aligned}I(x,y) &= (E_{r_0}\cos\theta_1 + E_{s_0}\cos\theta_2)^2 + i(E_{r_0}\sin\theta_1 + E_{s_0}\sin\theta_2)^2 \\ &= E_{r_0}^2 + E_{s_0}^2 + 2E_{r_0}E_{s_0}(\cos\theta_1\cos\theta_2 + \sin\theta_1\sin\theta_2)\end{aligned}$$

$$\therefore \qquad I(x,y) = E_{r_0}^2 + E_{s_0}^2 + 2E_{r_0}E_{s_0}\cos(\theta_1 - \theta_2)$$

writing $I(x,y)$ in terms of individual field intensities,

$$I(x,y) = I_{r_0} + I_{s_0} + 2\sqrt{I_{r_0}I_{s_0}}\cos\left(k(z_2 - z_1) + \xi(x,y)\right)$$

where, I_{r_0} and I_{s_0} are the maximum intensity amplitudes of the individual fields and $\Delta\theta = \theta_2 - \theta_1 = k(z_2 - z_1) + \xi(x, y)$ is their phase difference.

Further, considering $I_0 \equiv I_{r_0} = I_{s_0}$,

$$I(x, y) = 2I_0 \left[1 + \cos\left(k(z_2 - z_1) + \xi(x, y)\right)\right]$$

or,

$$I(x, y) = 4I_0 \cos^2\left[\frac{k(z_2 - z_1) + \xi(x, y)}{2}\right]$$

Appendix B

Examine the direction of motion of PZT mount

Experiments shown in Section 2.2.3 uses a Piezoelectric transducer (PZT) mount to linearly translate the sample over a fixed distance for calibration. However, its direction of motion, forward or backward along its translational axis, was not known. Following is the test performed to determine this.

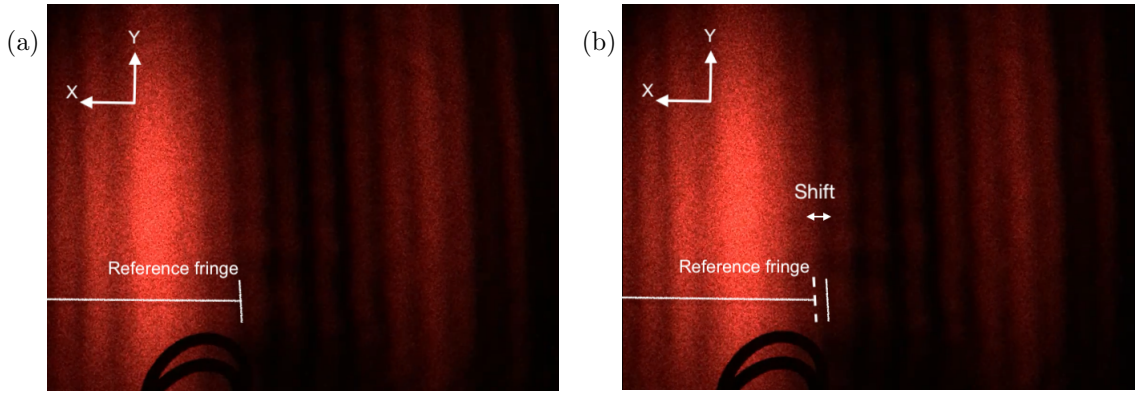

Figure B.1: **Tracking the diffraction pattern of a thin sample.** A net shift in $(-x)$-direction is seen for the fringes on comparing the images (a) before and (b) after the PZT mount is translated.

As shown in Fig. 2.1, the focused probe beam was used to shine over a silver microwire sample fixed vertically on the PZT mount. The mount was however rotated at 90 degrees to make its translational axis perpendicular to the incoming probe beam. A diffraction pattern was observed on a screen kept far away as the light passed about the thin sample. Now, the input voltage of the mount was increased from 0 to 149 V and the movement of the enlarged diffraction fringes was observed.

As the input voltage of the PZT mount is increased, the diffraction fringes are observed to move in the $(-x)$-direction on a screen placed orthogonal to the direction of propagation of light. This implies a similar behaviour of the PZT mount. Therefore, for a typical placement of the mount in the setup shown in Fig. 2.1, a positive voltage input in it results in the sample's translation along $(-z)$-direction and so on.

Bibliography

[1] Peter R. Griffiths and James A. de Haseth. *Fourier Transform Infrared Spectrometry*, chapter 5, pages 97–142. John Wiley and Sons, Ltd, 2006.

[2] John D Monnier. Optical interferometry in astronomy. *Reports on Progress in Physics*, 66(5):789–857, 2003.

[3] Alexander D. Cronin, Jörg Schmiedmayer, and David E. Pritchard. Optics and interferometry with atoms and molecules. *Rev. Mod. Phys.*, 81:1051–1129, 2009.

[4] K.J. Hemker and W.N. Sharpe. Microscale characterization of mechanical properties. *Annual Review of Materials Research*, 37(1):93–126, 2007.

[5] Pooja Munjal and Kamal P. Singh. A single-lens universal interferometer: Towards a class of frugal optical devices. *Applied Physics Letters*, 115(11):111102, 2019.

[6] William S. Trimmer. *Micromechanics and MEMS: Classic and Seminal Papers to 1990*. Wiley-IEEE Press, 1997. ISBN: 978-0-780-31085-8.

[7] M. Amanul Haque, Taher Saif, and William N. Sharpe (Ed.). *Springer Handbook of Experimental Solid Mechanics*. Springer, 2008. ch. 30, ISBN: 978-0-387-26883-5.

[8] O. Kraft and C. A. Volkert. Mechanical testing of thin films and small structures. *Advanced Engineering Materials*, 3(3):99–110, 2001.

[9] V. T. Srikar and S. M. Spearing. A critical review of microscale mechanical testing methods used in the design of microelectromechanical systems. *Experimental Mechanics*, 43(3):238–247, 2003.

[10] OpenWetWare. The benefits of small length scales in microscale systems - duy nguyen — openwetware,, 2018. [Online; accessed 25-April-2020].

[11] Robert W. Johnstone and M. Parameswaran. *An Introduction to Surface-Micromachining*. Kluwer Academic Publishers, 2004. ISBN: 978-1-4757-1077-9.

[12] M.A. Haque and M.T.A. Saif. A review of mems-based microscale and nanoscale tensile and bending testing. *Experimental Mechanics*, 43(3):248–255, 2003.

[13] Ting Yui Tsui. *Factors limiting the accuracy of mechanical-property measurement by nanoindentation*. PhD dissertation, Rice University, 1997.

[14] Stefan Johansson, Jan-Åke Schweitz, Lars Tenerz, and Jonas Tirén. Fracture testing of silicon microelements in situ in a scanning electron microscope. *Journal of Applied Physics*, 63(10):4799–4803, 1988.

[15] William N. Sharpe Jr., Bin Yuan, Ranji Vaidyanathan, and Richard L. Edwards. New test structures and techniques for measurement of mechanical properties of MEMS materials. In *Microlithography and Metrology in Micromachining II*, volume 2880, pages 78 – 91. SPIE, 1996.

[16] Svetlana Avramov-Zamurovic, Jae Myung Yoo, and Nicholas G. Dagalakis. Capacitive displacement sensor for detecting planar submicrometer motion. *Review of Scientific Instruments*, 87(6):065001, 2016.

[17] H.D Espinosa, B.C Prorok, and M Fischer. A methodology for determining mechanical properties of freestanding thin films and mems materials. *Journal of the Mechanics and Physics of Solids*, 51(1):47 – 67, 2003.

[18] Lin Qiu, Ning Zhu, Yanhui Feng, Efstathios E. Michaelides, Gaweł Żyła, Dengwei Jing, Xinxin Zhang, Pamela M. Norris, Christos N. Markides, and Omid Mahian. A review of recent advances in thermophysical properties at the nanoscale: From solid state to colloids. *Physics Reports*, 843:1 – 81, 2020.

[19] Sergey Edward Lyshevski. *Nano- and Micro-Electromechanical Systems*. CRC Press, 2005. ISBN: 978-1-4200-5793-5.

[20] A. A. Michelson and E. W. Morley. On the relative motion of the earth and the luminiferous ether. *American Journal of Science*, Series 3 Vol. 34(203):333–345, 1887.

[21] A. A. Michelson and E. W. Morley. Feasibility of establishing a light-wave as the ultimate standard of length. *American Journal of Science*, Series 3 Vol. 38(225):181–185, 1889.

[22] Artur G. Olszak, Joanna Schmit, and Monteith G. Heaton. Interferometric approaches each have advantages. www.laserfocusworld.com, 2001.

[23] Peter de Groot and Leslie Deck. Surface profiling by analysis of white-light interferograms in the spatial frequency domain. *Journal of Modern Optics*, 42(2):389–401, 1995.

[24] C. Corey Scott, Andreas Luttge, and Kyriacos A. Athanasiou. Development and validation of vertical scanning interferometry as a novel method for acquiring chondrocyte geometry. *Journal of Biomedical Materials Research Part A*, 72A(1):83–90, 2005.

[25] Leslie L. Deck, Peter J. de Groot, and James A. Soobitsky. Large-aperture, equal-path interferometer for precision measurements of flat transparent surfaces. *Appl. Opt.*, 53(8):1546–1553, 2014.

[26] Pooja Munjal and Kamal P. Singh. Optically probing picometer-resolved photodynamics of solid surfaces. *URSI Radio Science Bulletin*, 2019(370):12–16, 2019.

[27] Mitsuo Takeda, Hideki Ina, and Seiji Kobayashi. Fourier-transform method of fringe-pattern analysis for computer-based topography and interferometry. *J. Opt. Soc. Am.*, 72(1):156–160, 1982.

[28] Yu Fu, Giancarlo Pedrini, and Xide Li. Interferometric dynamic measurement: Techniques based on high-speed imaging or a single photodetector. *The Scientific World Journal*, 2014:232906, 2014.